



Separated flow around half-submerged horizontal circular cylinders at different Reynolds numbers

Samuel Addai¹ · Mark F. Tachie¹ · Karen Dow² · Shawn P. Clark² · Mark K. Israel¹

Received: 24 July 2023 / Revised: 2 November 2023 / Accepted: 16 November 2023 / Published online: 20 December 2023
© The Author(s), under exclusive licence to Springer-Verlag GmbH Germany, part of Springer Nature 2023

Abstract

Separated flow around floating pontoons, modeled using horizontal circular cylinders intersecting a free surface, is experimentally investigated using particle image velocimetry. Three different-sized cylinder geometries, i.e., small, medium and large cylinders are considered. The Reynolds numbers based on free-stream velocity and the cylinder diameter at which the geometries are tested range between 2880 and 25,510. The results show that as Reynolds number increases, the maximum back flow and the size of the recirculation bubble behind the small cylinder increase but remains almost constant for the medium and large cylinders. The distributions of the Reynolds stresses, turbulent kinetic energy and triple velocity correlations show concentrations along the mean dividing streamline with single peaks, and the magnitude of these peaks increase with increasing Reynolds number. Unlike the large cylinder, the peak locations of the Reynolds stresses and turbulent kinetic energy for the small cylinder shift upstream as Reynolds number increases, suggesting early transition to turbulence. Also, the combined contribution of the Reynolds shear stress to the total production of turbulence exceeds that from the Reynolds normal stresses. Moreover, the spatial coherence of the coherent structures decreases as Reynolds number increases.

1 Introduction

Flow past a partially submerged circular cylinder intersecting a free surface occurs in many engineering applications. A practical example is the flow around flexible hydraulic structures (booms) that are placed on the water surface to protect critical infrastructure. These booms are comprised of partially submerged horizontal cylindrical pontoons chained together that span the width of a channel upstream or downstream of a dam or other hydraulic structure. The ice boom,

for instance, is used to prevent ice from interacting with hydraulic structures, while also serving to be the bridging point for a solid ice cover to form. This is beneficial since a solid ice cover upstream of a structure will insulate the water and reduce subsequent ice formation throughout the winter.

When a circular cylinder is placed in a uniform flow, laminar flow separation occurs on the upper and lower sides of the cylinder, resulting in two separated shear layers in the cylinder wake. The separated shear layers evolve, undergo transition to turbulence, and roll up to entrain surrounding fluid downstream the cylinder (Arie et al. 1981; Bearman and Morel 1983; Lin et al. 1995; Perret 2009; Khabbouchi et al. 2014; Aljure et al. 2017). Consequently, a pair of mean recirculation bubbles, symmetric about the cylinder horizontal centerline, is formed in the wake (Qiu et al. 2022; Uruba 2022). The size of the bubbles is characterized using the mean recirculation length (L_r/D , where D is the cylinder diameter), defined as the streamwise distance from the mean flow separation point on the cylinder to the point along the cylinder horizontal centerline where the streamwise mean velocity is zero (Norberg 1998; Kim et al. 2015).

Past studies have shown that dimensionless parameters such as Reynolds number ($Re_D = U_e D/\nu$, where U_e corresponds to the free-stream velocity and ν is the kinematic viscosity of the working fluid), blockage ratio, and free-stream

✉ Mark F. Tachie
mark.tachie@umanitoba.ca

Samuel Addai
addais1@myumanitoba.ca

Karen Dow
karen.dow@umanitoba.ca

Shawn P. Clark
shawn.clark@umanitoba.ca

Mark K. Israel
israelm@myumanitoba.ca

¹ Department of Mechanical Engineering, University of Manitoba, Winnipeg, MB R3T 5V6, Canada

² Department of Civil Engineering, University of Manitoba, Winnipeg, MB R3T 5V6, Canada

turbulence intensity ($Tu = u'_{rms}/U_e$, where u'_{rms} is the root-mean-square value of the streamwise velocity fluctuation) influence the flow dynamics around a circular cylinder in a uniform flow (Norberg 1998; Khabbouchi et al. 2014). Table 1 summarizes some relevant studies on a circular cylinder in a uniform flow. For example, Norberg (1986) observed that the vortex formation length (L_f/D), defined as the streamwise location of peak vertical Reynolds normal stress measured from the mean flow separation points, decreases as free-stream turbulence intensity increased but increases with increasing Reynolds number. Contrary to the findings of Norberg (1986), Arie et al. (1981) reported an increase in the vortex formation length with increasing turbulence intensity.

Khabbouchi et al. (2014) conducted a study to examine the effects of free-stream turbulence intensity on the growth rate of separated shear layers originating from a circular cylinder in a uniform flow. They noted a consistent rise in the shear layer growth rate as the free-stream turbulence intensity increased. They also found that the location at which the shear layer growth rate suddenly increased, known as the point of transition to turbulence in the separated shear layers, moved upstream with an increase in turbulence intensity, resulting in a shortened recirculation length.

When a cylinder is positioned near a solid wall, it is subjected to wall turbulence and mean shear, causing the pair of mean recirculation bubbles in the wake to no longer be symmetric around the cylinder horizontal centerline (Zdravkovich 1985; Price et al. 2002; Wang and Tan 2008). The boundary layer on the wall interacts with the lower separated shear layer from the cylinder, restricting its growth (Taniguchi and Miyakoshi 1990; Zovatto and Pedrizzetti 2001; Bhattacharyya and Maiti 2004; Thompson et al. 2020). Furthermore, the proximity of the wall leads to an increase in the recirculation length and a reduction in the Reynolds stresses for a cylinder in the vicinity of a wall compared to a cylinder in a uniform flow (Duraio et al. 1991; Wang and Tan 2008; Addai et al. 2022). For a wall-mounted cylinder, i.e., a cylinder in direct contact with a wall, however, only

one large mean recirculation bubble is formed in the wake. The von Kármán vortices are suppressed and can no longer be observed (Lei et al. 1999; Martinuzzi et al. 2003).

The flow characteristics around a cylinder intersecting a free surface at low Froude numbers ($Fr_H = U_e/\sqrt{gH}$, where $g = 9.81 \text{ m/s}^2$ is the acceleration due to gravity) displays some behaviors common to the flow around a wall-mounted cylinder such as the formation of a single recirculation bubble in the cylinder wake which tends to increase in size as Reynolds number increases (Reichl et al. 2003). Unlike the flow around a wall-mounted cylinder, the onset of vortex formation is delayed for a cylinder intersecting a free surface due to free surface distortion (Sheridan et al. 1997). The free surface alters the flow dynamics, making the flow remarkably more complex than that of a cylinder in a uniform flow. Thus, in addition to Reynolds number and free-stream turbulence intensity, the Froude number (Fr_H) may also affect the vortex dynamics considerably.

Depending on the extent to which the cylinder is submerged below the free surface, different submergence ratios (S/D), defined as the ratio of the submerged depth of the cylinder (S) to the diameter of the cylinder, can be considered. Previous studies on a partially submerged circular cylinder at a fixed S/D of 0.5, which is the focus of the present study, are summarized in Table 2.

Triantafyllou and Dimas (1989) studied the flow around a half-submerged circular cylinder using linear stability analysis at Froude numbers in the range $0 \leq Fr_H \leq 2.5$ and validated the results using experimental data at $Re_D = 50,000$. At low Froude numbers of $Fr \leq 0.5$, they showed that the flow is steady and attributed such an observation to the suppression of unsteady effects by the free surface. As Froude number was further increased, they observed strong oscillation in the flow and large amplitude waves on the free surface. Their experimental result, which was performed at $Fr_H = 0.65$, showed a mean recirculation length of $L_r/D = 2.5$. Bouscasse et al. (2015) numerically investigated the flow past a half-submerged circular cylinder at a low Reynolds number of $Re_D = 180$ and Froude numbers of

Table 1 Studies on circular cylinders in uniform flow

Author	Measurement	Re_D	Tu (%)	L_r/D
Maekawa and Mizuno (1967)	HWA ^a	37,000–280,000	–	–
Arie et al. (1981)	PM ^b , HWA	7900–54,000	1.0–15.80	–
Norberg (1986)	PM, HWA	20,000–60,000	1.30–4.10	–
Hammache & Gharib (1989)	FV ^c	72–158	–	–
Norberg (1998)	LDV ^d	1500–10,000	0.1	1.5–2.3
Perret (2009)	PIV ^e	12,500	0.5	0.83
Khabbouchi et al. (2014)	HWA	4500–47,000	0.25–6.20	–
Aljure et al. (2017)	DNS ^f	5000	–	1.7

^aHot-wire anemometry, ^bpressure measurements, ^cflow visualization, ^dlaser Doppler velocimetry, ^eparticle image velocimetry, ^fdirect numerical simulation

Table 2 Studies on flow past half-submerged circular cylinders

Author	Measurement	Re_D	Tu (%)	L_r/D	Fr_H
Triantafyllou and Dimas (1989)	LSA	50,000	–	2.5	0–2.50
Lin et al. (1996)	PIV	2855	–	–	0.32
Sheridan et al. (1997)	PIV	5990–9120	–	–	0.47–0.72
Bouscasse et al. (2015)	SPH	180	–	0.3–2.0	0.48, 0.50
Edie et al. (2021)	PIV	2875–8588	6.6–9.5	–	0.22–0.65
Edie (2022)	PIV	2882–25,509	0.72–1.08	0.2–2.5	0.22–0.38

$Fr_H = 0.48$ and 0.50 using smoothed particle hydrodynamics method. They found the flow to be steady at $Fr_H = 0.48$, which is consistent with the earlier study by Triantafyllou and Dimas (1989). When the Froude number was increased to $Fr = 0.5$, the flow moved over the top side of the cylinder, forming a jet. Although separated shear layers were formed on the upper and lower sides of the cylinder in this case, the von Kármán vortex shedding was absent. Lin et al. (1996) also conducted an experimental study on the flow around a half-submerged circular cylinder at $Re_D = 2855$ and $Fr = 0.32$. They observed a concentration of the spanwise vorticity along the lower separated shear layer, however, the free surface inhibited the formation of von Kármán vortices which are a salient feature of the wake of a cylinder in a uniform flow.

Edie et al. (2021) and Edie (2022) investigated the flow around a submerged cylinder at Reynolds numbers of $2,880 \leq Re_D \leq 8,650$ and at submergence ratios of $S/D = 0.3, 0.5$ and 0.7 . The results were analyzed in terms of the mean flow, Reynolds stresses and triple velocity correlations. With increasing Reynolds number, they observed an increase in the magnitudes of the maximum back flow and the streamwise Reynolds normal stress. The vertical Reynolds normal stress and Reynolds shear stress, however, were weakly dependent on Reynolds number. It was also observed that the recirculation length increased with increasing Reynolds number, submergence ratio and Froude number.

This study models turbulent flows around ice booms. Booms face a variety of forces throughout their service life, including the frictional and drag forces initiated by the separating turbulent flow immediately downstream of the pontoons. These have, unfortunately, resulted in a number of boom failures, which increase the safety risk at the structure they were designed to protect. In spite of these, the turbulent flow characteristics around these booms remains to be understood due to the limited research conducted on separated flows induced by partially submerged cylinders compared to the fully immersed case. Therefore, the objective of the present study is to investigate the wake characteristics of partially submerged circular cylinders of different sizes and at relatively high Reynolds numbers to provide additional information to help with future boom design. Specifically, this study complements the study by Edie (2022) examining

the effects of Reynolds number on the mean flow, Reynolds stresses and turbulent transport of the turbulent kinetic energy and assesses Reynolds number effects on turbulent kinetic energy budget terms and on the dynamics of large-scale structures in the wake of the partially submerged cylinders—areas that have not been explored in previous studies. The rest of the paper is organized as follows: the experimental setup and measurement procedure are described in Sect. 2, the results are presented and discussed in Sect. 3. Finally, the major findings and conclusions are summarized in Sect. 4.

2 Experimental setup and measurement procedure

The study was conducted at the Turbulence and Hydraulic Engineering Laboratory (THEL) at the University of Manitoba, where an open recirculating water channel with a streamwise length of 6000 mm, vertical height of 450 mm, and spanwise width of 600 mm was used. The test section consisted of two side walls and a bottom wall, which were made from 31.8 mm thick Super Abrasion Resistant® transparent acrylic plates to enable optical access to the flow. A pump which is regulated by a 30-kW variable-speed motor was used to drive the recirculating water.

A schematic of the test section, cylinder, and Cartesian coordinate system used in the study is shown in Fig. 1. The x - and y - coordinates represent the streamwise and vertical directions, respectively, and their corresponding origins were set at the cylinder center point. The cylinder had a spanwise width (W) of 588 mm and was installed between two 6-mm thick acrylic plates with a skew angle of 45° machined at the leading edges to suppress distortion of the flow near the channel mid-span. The streamwise extent of each acrylic plate was 830 mm and the leading edges of the plates were 480 mm upstream of the cylinder center point. As shown in Fig. 1, the water depth (H) was maintained at 400 mm and the cylinder was held in a stationary position by a rod and angle assembly such that only the bottom half of the cylinder was below the free surface of the water, i.e., cylinder was half-submerged ($S/D = 0.5$) in the flow. To reduce

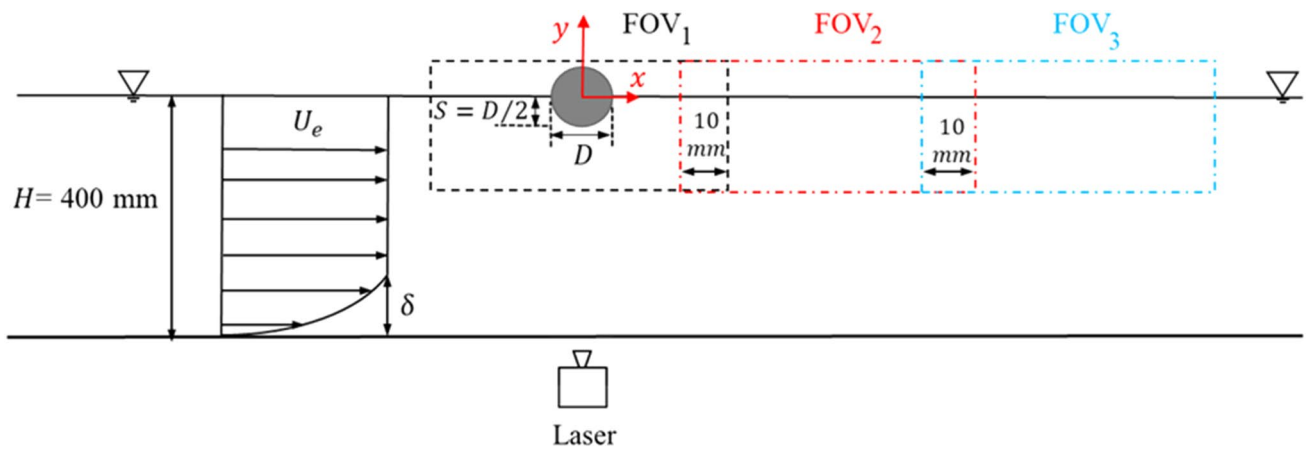


Fig. 1 Schematic of the experimental set-up, the adopted coordinate system, and the fields of view (FOVs) of the cameras. The cylinder diameter, water depth, free-stream velocity and boundary layer thickness are denoted by D , H , U_e and δ , respectively

surface glare caused by laser illumination, a non-reflective black paint was applied to the middle parts of the cylinder.

Cylinders with diameters of 26.2 mm, 51.5 mm and 77.3 mm, hereinafter, referred to as small, medium, and large cylinder geometries, respectively, were examined in the present experiments. For each geometry, three free-stream velocities, $U_e = 0.11$ m/s, 0.22 m/s, and 0.33 m/s were tested yielding a total of nine test cases. The room temperature was kept at 20 °C, and the kinematic viscosity of water was $\nu = 10^{-6}$ m²/s. Table 3 summarizes the various test cases and some pertinent parameters such as the Reynolds number, Froude numbers (Fr_H and $Fr_S = U_e/\sqrt{gS}$, where $S = D/2$), blockage ratio (S/H) and the free-stream turbulence intensity (Tu). The test notation adopted for each case is such that the letter corresponds to the cylinder geometry (small, medium, or large) whereas the subscript corresponds to the Reynolds number. For example, S_{2880} corresponds to experiment at a Reynolds number of 2800 using the small cylinder. From the table, Fr_H and Fr_S , respectively, ranged from 0.06 to 0.17, and 0.18 to 0.92, while the turbulence intensity and blockage ratio ranged from 0.69 to 1.1% and 3.3 to 9.7%, respectively.

A planar particle image velocimetry (PIV) system was used to perform detailed velocity measurements in x - y plane at the channel mid-span, with the flow seeded with 10 μ m silver-coated hollow glass spheres having a specific gravity of 1.4. The slip velocity (u_s) was calculated using the expression:

$$u_s = \frac{d_p^2(\rho_p - \rho_f)g}{18\rho_f\nu} \tag{1}$$

Here, d_p is the diameter of the seeding particles, ν is the kinematic viscosity of water at 20 °C, ρ_p and ρ_f denote the densities of the seeding particles and water, respectively. The value of u_s was 2.18×10^{-5} m/s. To quantify the response time of the seeding particles to sudden changes in the flow velocity, the relaxation time ($\tau_p = u_s/g$) was estimated to be 2.20×10^{-6} s while the characteristic time scales ($\tau_f = D/U_e$) ranged from 0.079 to 0.703 s.

The values of the Stokes number ($S_k = \tau_p/\tau_f$) were between 3.13×10^{-6} and 2.77×10^{-5} . These values are significantly lower than the recommended threshold value of $S_k = 0.05$ below which the seeding particles faithfully follow

Table 3 Summary of the different test cases and some relevant parameters

Test cases	D (mm)	U_e (m/s)	Re_D	Fr_H	Fr_S	S/H (%)	Tu (%)
S_{2880}	26.20	0.11	2,880	0.06	0.31	3.3	0.69
S_{5760}		0.22	5,760	0.11	0.61	3.3	0.75
S_{8650}		0.33	8,650	0.17	0.92	3.3	1.10
M_{5670}	51.50	0.11	5,670	0.06	0.22	6.4	0.69
M_{11330}		0.22	11,330	0.11	0.44	6.4	0.75
M_{17000}		0.33	17,000	0.17	0.66	6.4	1.10
L_{8500}	77.30	0.11	8,500	0.06	0.18	9.7	0.69
L_{17000}		0.22	17,000	0.11	0.36	9.7	0.75
L_{25510}		0.33	25,500	0.17	0.54	9.7	1.10

the flow of fluid (Samimy and Lele 1991). The particles were illuminated using a dual-cavity high-speed neodymium-doped yttrium lithium fluoride (Nd: YLF) laser that emits green light (wavelength = 527 nm) up to a maximum pulse energy of 30 mJ/pulse. The thickness of the laser light sheet was roughly 1 mm, and 12-bit complementary metal oxide semiconductor (CMOS) cameras with a full resolution of 2560 pixel × 1600 pixel were positioned next to each other to capture the illuminated flow field. For the small cylinder geometry, two cameras were employed whereas three cameras were used to capture the flow regions of interest for the medium and large cylinder geometries. The fields of view (FOVs) of any two adjacent cameras overlapped by about 10 mm in the streamwise direction which yielded an overall FOV of $(x \times y) = (14.4 D \times 4.5 D)$, $(11.1 D \times 2.3 D)$ and $(7.3 D \times 1.5 D)$ for the small, medium, and large cylinders, respectively. To obtain statistically independent samples, the cameras were operated at a frame rate of 3 Hz and a total of 3000 velocity vector fields were captured for each test case.

Data acquisition and velocity vector calculation were carried out using DaVis version 10, a commercial software provided by LaVision Inc. In order to minimize peak locking, the particle image diameter was maintained between 2 and 4 pixels for all measurements. The velocity vectors were calculated using a multi-pass cross-correlation algorithm that was accelerated by a graphical-processing-unit (GPU). The data was processed using an initial pass with an interrogation area of 64 pixel × 64 pixel with 50% overlap. This was followed by three passes using an interrogation area of 32 pixel × 32 pixel with 75% overlap.

The streamwise and vertical mean velocities are hereafter denoted by U and V , respectively, while u' and v' denote the corresponding fluctuating velocities. The measurement uncertainties in the mean velocities and Reynolds stresses for statistically independent samples are quantified following studies by Sciacchitano and Wieneke (2016) and Bendat and Piersol (2010). Within a confidence level of 95% and using a confidence coefficient of $Z_c = 1.96$, the uncertainties in the mean velocities and Reynolds stresses are estimated to be $\pm 0.37\%$ and $\pm 3.62\%$, respectively, in the uniform flow. At locations of peak streamwise Reynolds normal stress for test cases S_{8650} , M_{5670} and L_{25510} , however, the maximum uncertainties in the mean velocities and Reynolds stresses are estimated to be $\pm 1.9\%$ and $\pm 7.23\%$, respectively, due to elevated local turbulence levels.

3 Results and discussion

3.1 Mean flow

In this section, we evaluate the effects of Reynolds number and blockage ratio on the mean flow characteristics around a partially submerged horizontal circular cylinder. Figures 2 and 3 illustrate the contours of normalized streamwise and vertical mean velocities, superimposed with mean streamlines, for all test cases. The red dashed lines on Figs. 2 and 3, respectively, represent the isopleths of $U = 0$ and $V = 0$. The isopleth of $U = 0$ encompasses the region of flow reversal ($U < 0$) and provides a measure of the mean recirculation

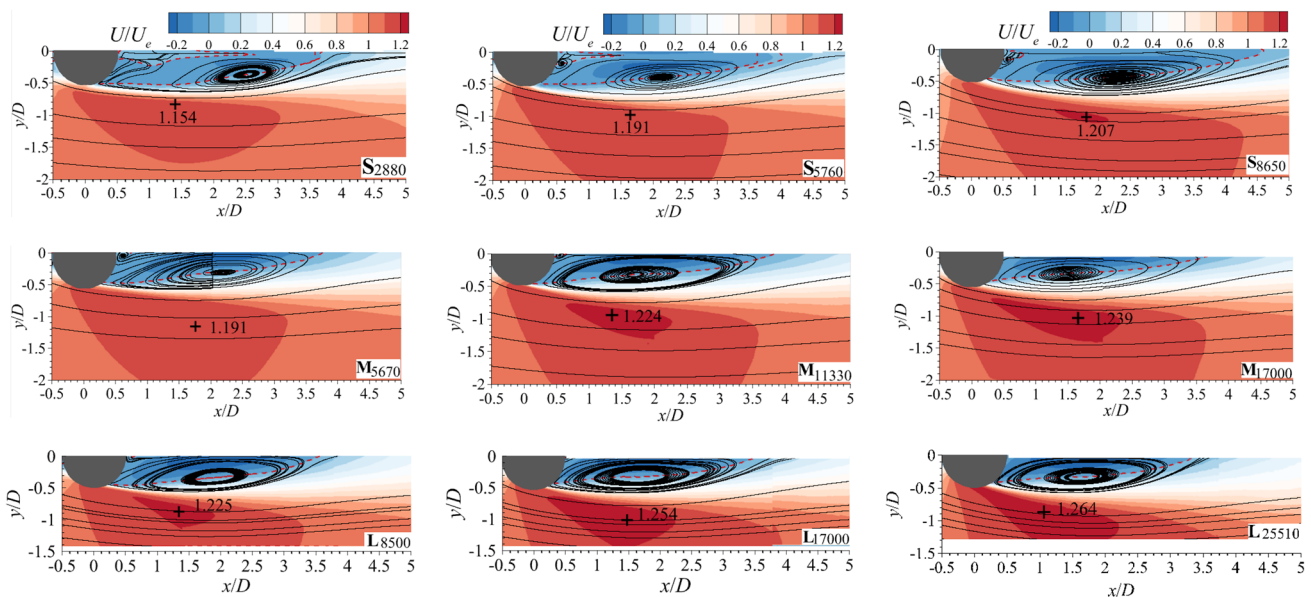


Fig. 2 Contours of streamwise mean velocity for all test cases. The red dashed line is the isopleth of zero- mean streamwise velocity ($U = 0$). The magnitudes of the maximum streamwise mean velocity

are shown on the contours and their respective locations are marked by the plus “+” symbol

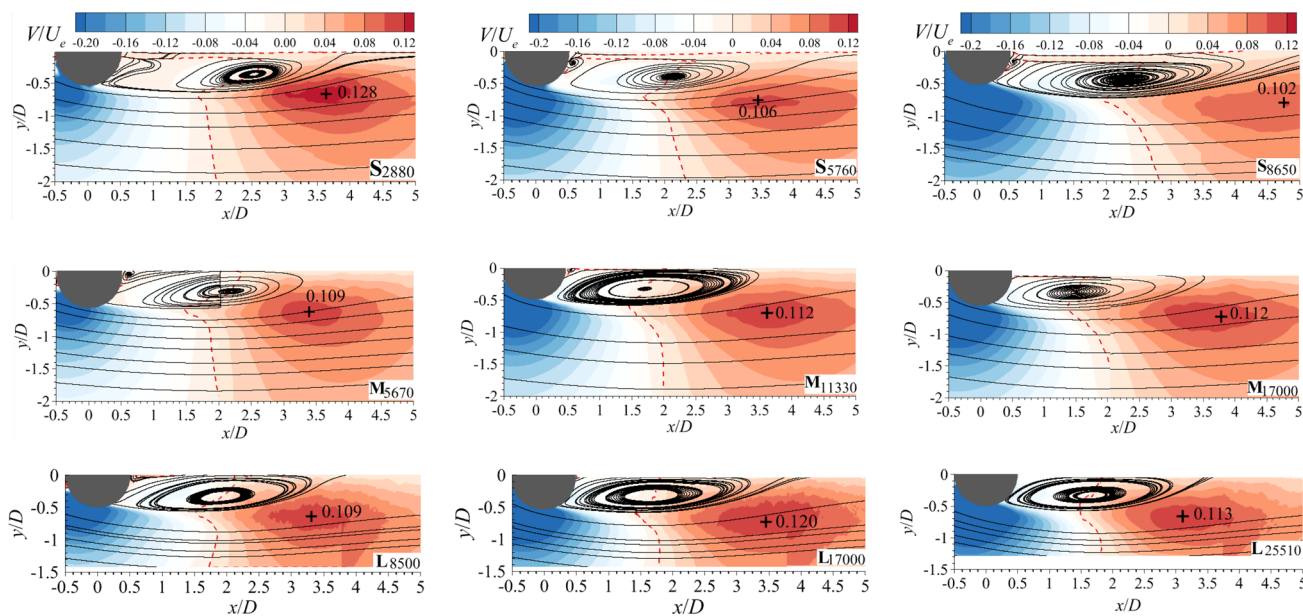


Fig. 3 Contours of vertical mean velocity for all test cases. The red dashed line is the isopleth of zero-mean vertical velocity ($V = 0$). The magnitudes of the maximum vertical mean velocity are shown on the contours and their respective locations are marked by the plus “+” symbol

length while the isopleth of $V = 0$ demarcates the regions of downward and upward mean flow deflections. The contours show that the reduced flow section below the cylinders results in the acceleration of the approach flow around the cylinders. The local maxima of mean flow velocities are indicated on the plots and their respective locations are marked by the “+” symbol. The figures also show that the mean flow deflects downwards upon interaction with the cylinder, separates on the lower side of the cylinder, and subsequently deflects upwards towards the free surface, forming mean recirculation bubbles in the wake. The mean recirculation bubbles are characterized by a large counter-clockwise rotating primary vortex and a small clockwise rotating secondary vortex which forms at the intersection of the cylinder and the free surface. In the present study, however, the small vortex was not distinctly resolved at relatively low ($Re = 2880$) and high ($Re \geq 17,000$) Reynolds numbers due to weak velocity and free surface deformation, respectively.

As Reynolds number increases, the separated shear layer travels further downstream before reattaching to the free surface for the small cylinder. Hence, the size of the recirculation bubble increases, as observed from Figs. 2 and 3. Additionally, the streamwise location of the vortex core shifts upstream with increasing Reynolds number. Specifically, the streamwise location of the vortex core at S_{2880} is $x/D = 2.54$ but shifts upstream to $x/D = 2.28$ at S_{8650} .

Figure 4 presents a quantitative assessment of the effects of Reynolds number on the maximum streamwise mean velocity (U_{max}), the maximum backflow velocity in the recirculation region (U_b), the streamwise location of the

vortex core (x_c), and the size of the mean recirculation bubble. The results are compared with findings of some previous studies, as shown in the figure. Figure 4a and b show the variation of the magnitudes of U_{max}/U_e and U_b/U_e with Reynolds number, respectively. The maximum streamwise mean velocity tends to increase with increasing Reynolds number for all cylinder geometries, as observed from Fig. 4a. At similar Reynolds numbers (S_{8650} and L_{8500}) and (M_{17000} and L_{17000}), the maximum streamwise mean velocity for the larger cylinder is approximately 1.49% and 1.21% larger than the corresponding values for the small and medium cylinders, respectively. Since these differences are within measurement uncertainty, it is concluded that the maximum streamwise mean velocity is not significantly affected by changes in blockage ratio resulting from increase in size of the cylinder.

The variation of maximum streamwise mean velocity with Reynolds number is described using the correlation: $U_{max}/U_e = 1.39[0.587/(1 + (Re_D/1151)^{0.41})]$, which fits the data with an R-squared value of 0.97 (Fig. 4a). The magnitude of the maximum back flow (U_b/U_e) for the small cylinder increases with increasing Reynolds number, but for the medium and large cylinders, it does not vary significantly with Reynolds number and is approximately $U_b/U_e = 0.27$ and 0.33 , respectively. Moreover, the maximum back flow tends to increase with increasing cylinder size at comparable Reynolds numbers. For instance, the value of U_b/U_e for M_{5670} is 8.3% higher than that of S_{5760} , while that of L_{8500} is 32.6% higher than the corresponding value for S_{8650} . The average magnitude of $U_b/U_e = 0.33$ for the large cylinder

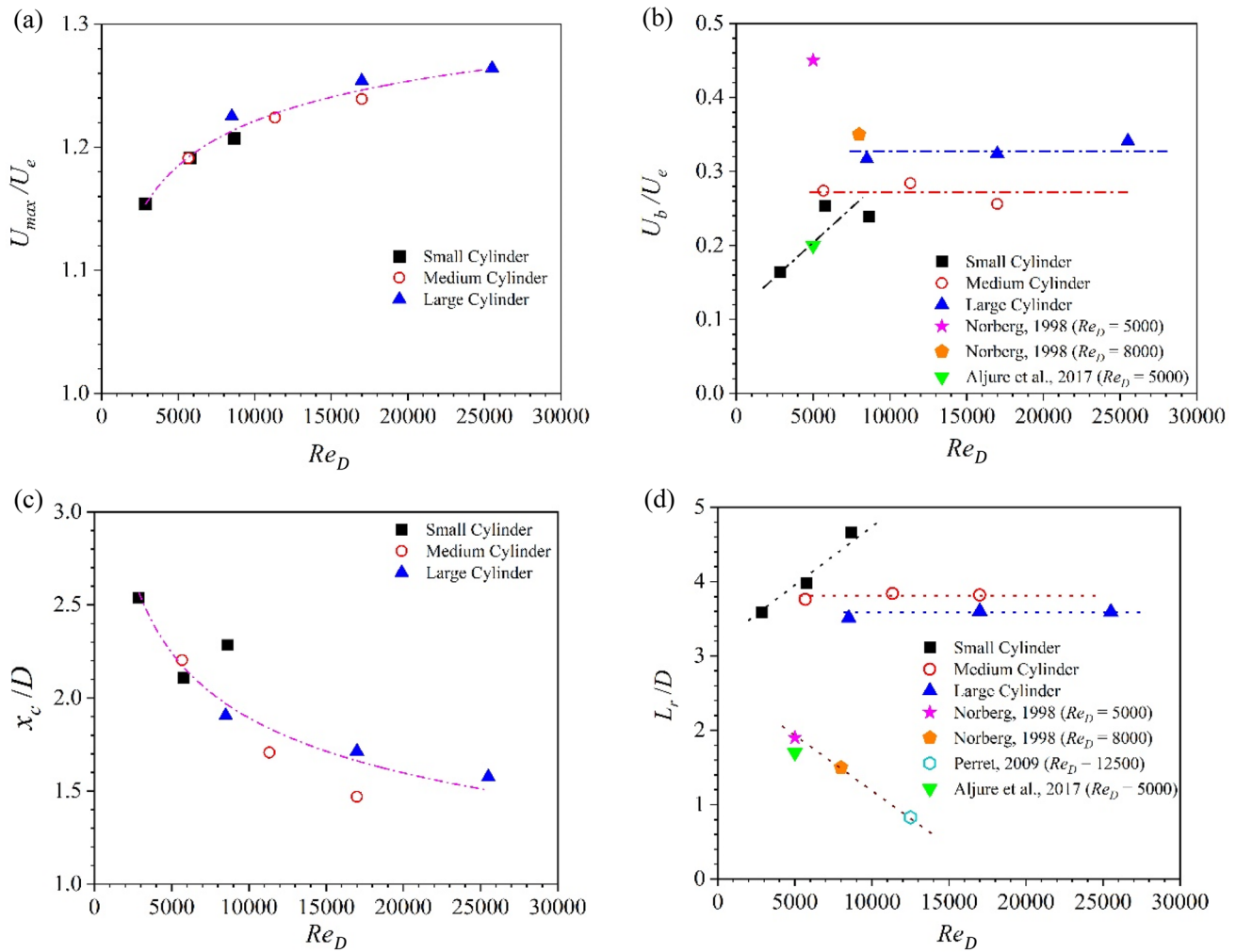


Fig. 4 Plot of **a** maximum streamwise mean velocity (U_{max}/U_e), **b** maximum back flow (U_b/U_e), **c** streamwise location of vortex core (x_c/D) and **d** recirculation length (L_r/D) versus Reynolds number (Re_D)

is 5.7% and 26.7% lower than those reported by Norberg (1998) at $Re_D = 8000$ and Norberg (1998) at $Re_D = 5000$, respectively for a circular cylinder in a uniform flow.

For each cylinder geometry in Fig. 4c, the streamwise distance between the cylinder center point and the vortex core in the wake is observed to reduce with increasing Reynolds number and follows the correlation: $x_c/D = 18.1(Re_D^{-0.25})$ which fits the data with an R-squared value of 0.83. Figure 4d plots the mean recirculation lengths, measured from the center of the cylinder, i.e., $(x/D, y/D) = (0, 0)$, to the point where the isopleth of $U = 0$ intersects the free surface, for the present and past studies versus Reynolds number. For the small cylinder, L_r/D monotonically increases with Re_D unlike the medium and large cylinders which are nearly independent of Reynolds number with average values of 3.5 and 3.8, respectively. This suggests that L_r/D is sensitive to Re_D at relatively low Reynolds number in the subcritical regime. The sensitivity

of the recirculation length to Reynolds number at relatively low Reynolds number is consistent with previous study by Zdravkovich (1997) on a circular cylinder in a uniform flow. However, in their case, the recirculation length rather decreased with increasing Reynolds number. As shown in Fig. 4d, the mean recirculation length of a circular cylinder in a uniform flow reported by Norberg (1998), Perret (2009) and Aljure et al. (2017) decreases monotonically as Reynolds number increases, which is contrary to the present finding. It is noted that, for a forward-facing step, Essel et al. (2015) and Sherry et al. (2009) reported an increase in reattachment length with increasing Reynolds number based on the step height (Re_h) at relatively low Reynolds numbers ($Re_h < 6300$ in Essel et al. (2015) and $Re_h < 8500$ in Sherry et al. (2009)); however, the reattachment length was independent of Reynolds number at higher Reynolds numbers, which is in good agreement with the present study.

At selected streamwise locations downstream of the cylinder center point (i.e., $x/D = 1, 2, 3$ and 4) for test cases S_{5760} , S_{8650} , L_{8500} and L_{17000} , vertical profiles of the streamwise and vertical mean velocities are extracted to quantitatively assess the evolution of the mean flow, and also examine Reynolds number and blockage effects on the wake flow, as shown in Fig. 5. For conciseness, profiles for the medium cylinder are omitted since they are similar to those of the other two geometries. For example, the profiles of M_{5670} and M_{17000} collapsed onto those of S_{5760} and L_{17000} , respectively. From Fig. 5, the flow is significantly distorted immediately downstream of the cylinder but gradually redevelops with increasing streamwise distance. The profiles of S_{8650} show the slowest flow recovery due to significant downward deflection of the flow, resulting in relatively large area of flow reversal. At $x/D = 1$, the U profiles of S_{5760} and L_{8500} are almost identical unlike the V profiles. With increasing streamwise distance to $x/D = 2$ and 3 , however, the recovery of the U profile for L_{8500} compared with S_{5760} is delayed. On the other hand, the recovery of V profile for S_{5760} relative to that of L_{8500} is consistently delayed as streamwise distance increases.

3.2 Reynolds stresses and turbulent kinetic energy

The effects of Reynolds number and blockage ratio on the fluctuating velocity field around the cylinders are examined using the distributions of Reynolds stresses and turbulent kinetic energy. For a circular cylinder in a uniform flow, the streamwise Reynolds normal stress and Reynolds shear stress are concentrated along the separated shear layers, resulting in dual peaks. Meanwhile, the vertical Reynolds

normal stress is concentrated along the cylinder horizontal centerline with a single peak. Figure 6 presents contours of streamwise $(\overline{u'u'}/U_e^2)$ and vertical $(\overline{v'v'}/U_e^2)$ Reynolds normal stresses around the submerged cylinders. For conciseness, only selected test cases are shown owing to similarity in the flow pattern for the various test cases. The peak magnitudes of the Reynolds stresses as well as their respective locations (marked by “+” symbol) are shown on the contours. The solid black line on the plots corresponds to the mean dividing streamline.

The distributions of the streamwise Reynolds normal stress show concentration along the mean dividing streamline in agreement with observations made for a circular cylinder in a uniform flow. Nonetheless, only a single peak is observed in contrast to the dual peaks observed in the wake of a cylinder in a uniform flow due to the absence of an upper separated shear layer in the present study. At the lowest Reynolds number for the small cylinder (i.e., S_{2880}), a region of elevated Reynolds stress does not appear until $x/D \approx 1.5$. As Reynolds number increases, this region as well as the peak location of $\overline{u'u'}$ shifts upstream. This is consistent with observation that for circular and rectangular cylinders, transition to turbulence occurs sooner at higher Reynolds numbers (Brun et al. 2008; Lander et al. 2018; Moore et al. 2019).

In contrast to a cylinder in a uniform flow, a region of elevated $\overline{v'v'}/U_e^2$ and its local peak occur along the separated shear layer. This is not surprising since the occurrence of $\overline{v'v'}$ along the centerline in the near wake of a cylinder in a uniform flow is associated with the high vertical velocity fluctuations resulting from the formation of the von Kármán vortex street, a phenomenon that is absent in partially

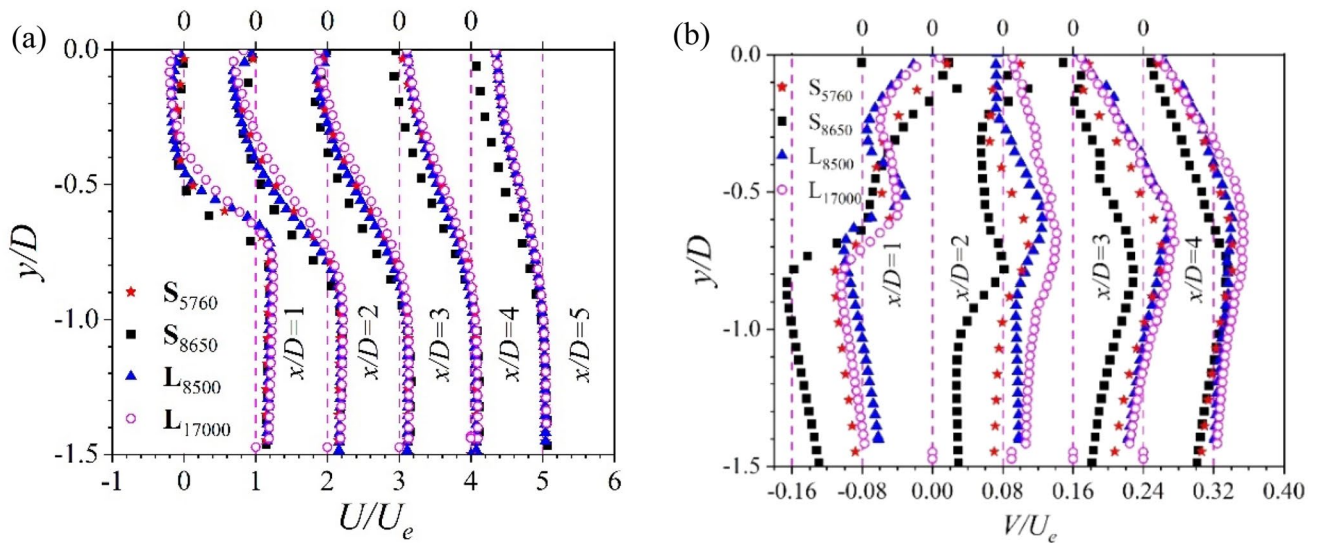


Fig. 5 Vertical profiles of a streamwise and b vertical mean velocities for selected test cases. For each test case, the profiles at the various streamwise locations are shifted to the right along the horizontal axis for clarity

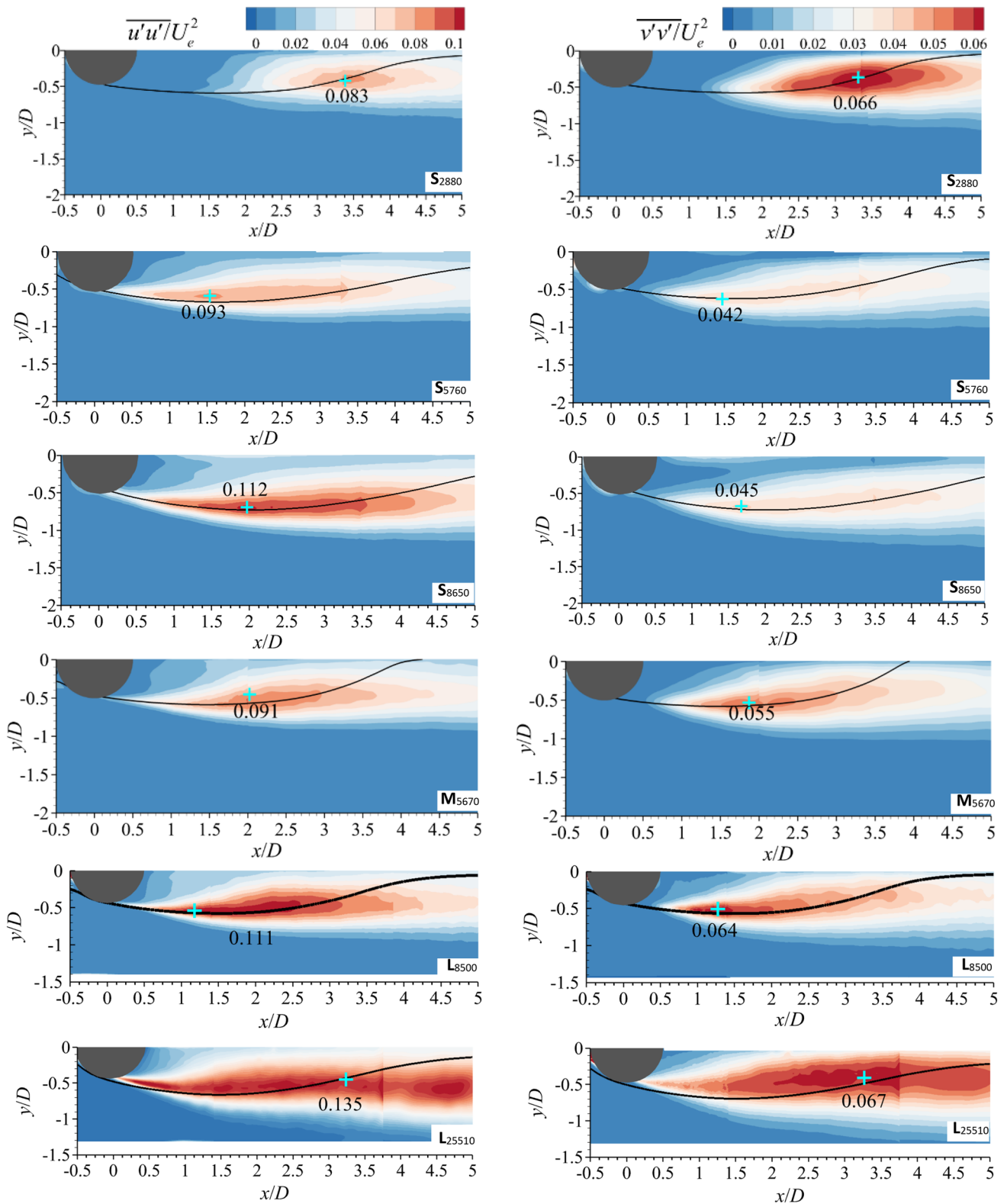


Fig. 6 Contours of streamwise (left) and vertical (right) Reynolds normal stresses for selected test cases. The magnitudes of the peak Reynolds normal stresses are shown on the contours and their respec-

tive locations are marked by the plus “+” symbol. The black solid is the mean dividing streamline

submerged circular cylinders. The results also show that the levels of the vertical Reynolds normal stress are significantly lower than the streamwise counterpart which highlight the anisotropic nature of turbulent flow around partially submerged circular cylinders. The peak location of the vertical Reynolds normal stress for the small cylinder also moves upstream at higher Reynolds number, as was observed for the streamwise Reynolds normal stress. Contrary to the upstream shift of the peak location of streamwise Reynolds normal stress for the small cylinder, the peak location of the vertical Reynolds normal stress for the large cylinder shifts downstream as Reynolds number is increased.

Contours of Reynolds shear stress ($\overline{u'v'}/U_e^2$) and turbulent kinetic energy (TKE) are shown in Fig. 7. Since the spanwise velocity fluctuation was not measured in the present study, the turbulent kinetic energy was estimated as $\text{TKE} = 0.5 (\overline{u'u'} + \overline{v'v'})$. Similar to the distributions of the Reynolds normal stresses, the Reynolds shear stress and TKE are concentrated along the mean dividing streamline with single peaks. Also, the peak locations of the Reynolds shear stress and TKE coincide with those for the Reynolds normal stresses (Fig. 6). For each test case, the peak magnitude of $\overline{u'v'}/U_e^2$ is consistently lower than any of the Reynolds normal stresses. For the small cylinder, the peak magnitude of $\overline{u'v'}/U_e^2$ decreases with increasing Reynolds number while for the large cylinder, $\overline{u'v'}/U_e^2$ is enhanced as Reynolds number increases. The distribution of TKE for both the small and large cylinders shows an increase in the peak magnitudes as Reynolds number increases, in conformity with the trend observed for the streamwise Reynolds normal stress since it is the major contributor to TKE (Fig. 7).

The variation of the peak magnitudes of the turbulent intensities (u'_{rms}/U_e and v'_{rms}/U_e) and TKE with Reynolds number is examined in Fig. 8. Data from previous studies are also plotted for comparison. From Fig. 8a, the peak magnitudes of the streamwise turbulent intensity (u'_{rms}/U_e) in the present study tend to increase with increasing Reynolds number and follows the correlation: $u'_{rms}/U_e = 0.116(Re_D^{0.11})$ which fits the data with an R-squared value of 0.86 in spite of the slight deviations. The peak magnitudes reported by Norberg (1998) for a cylinder in a uniform flow at Reynolds number $Re_D = 5000$ are about 16% and 11% higher than those for M_{5670} and S_{5760} , respectively. The peak magnitudes of the vertical turbulence intensity (v'_{rms}/U_e) and TKE also tend to increase with Reynolds number, as shown in Fig. 8b and c, respectively.

Figure 9 presents vertical profiles of the Reynolds stresses at various streamwise locations downstream the cylinder ($x/D = 1, 2, 3$ and 4) for selected test cases S_{5760} , S_{8650} , L_{8500} and L_{17000} . Generally, the Reynolds stresses are significantly enhanced immediately downstream of the cylinder but decay with increasing streamwise distance. The y -locations at which the peak magnitudes occur tend to shift

upwards as streamwise distance downstream the cylinder increases. Also, for each cylinder geometry, the magnitudes of the Reynolds stresses are observed to increase with increase in Reynolds number. At comparable Reynolds numbers (S_{8650} and L_{8500}), the Reynolds normal stresses for S_{8650} are consistently higher in magnitude than those of L_{8500} at each streamwise location unlike what is observed from the Reynolds shear stress profiles.

3.3 Turbulent transport of turbulent kinetic energy

Spatial topology of the triple velocity correlations has been used in previous investigations of turbulent shear flows to provide insight into turbulent transport of Reynolds stresses and turbulent kinetic energy. In particular, $(\overline{u'u'u'} + \overline{v'v'u'})$ measures the transport of the instantaneous turbulent kinetic energy ($u'u' + v'v'$) by u' whereas $(\overline{u'u'v'} + \overline{v'v'v'})$ corresponds to the transport of instantaneous turbulent kinetic energy ($u'u' + v'v'$) by v' . As shown in Fig. 10, the triple velocity correlations are concentrated along the separated shear layer, similar to the Reynolds stresses. The distributions of $(\overline{u'u'u'} + \overline{v'v'u'})$ and $(\overline{u'u'v'} + \overline{v'v'v'})$ both show a positive region close to the free surface and a negative region below the mean dividing streamline. Since $u'u'$ and $v'v'$ are both positive, the positive region adjacent to the free surface suggests sweep events ($u' > 0$ and $v' > 0$) or transport of TKE along the separated shear layer by high-speed fluid towards the free surface. Meanwhile, the negative region beneath the separated streamline is due to ejection events ($u' < 0$ and $v' < 0$) which is consistent with transport of turbulence by low-speed fluid downwards into the free stream. The transport of TKE by streamwise fluctuating velocity ($\overline{u'u'u'} + \overline{v'v'u'}$) is comparatively more intense than by the vertical fluctuating velocity ($\overline{u'u'v'} + \overline{v'v'v'}$), irrespective of the test condition. Also, turbulence transport by ejection events (negative region below the mean separated streamline) exceeds transport by sweep events. Similar to the Reynolds stresses and TKE (Figs. 6, 7), the level of turbulence transport increases with increasing Reynolds number, and an increase in blockage ratio results in higher levels of turbulence transport.

3.4 Budget terms of turbulent kinetic energy

The budget terms in the transport equation of the turbulent kinetic energy (TKE) are used to highlight turbulence production, and transport by the mean flow and fluctuating velocities. When the flow is statistically steady, the transport equation for TKE (k) can be expressed as:

$$0 = P_k + C_k + D_k + \epsilon_k, \quad (2)$$

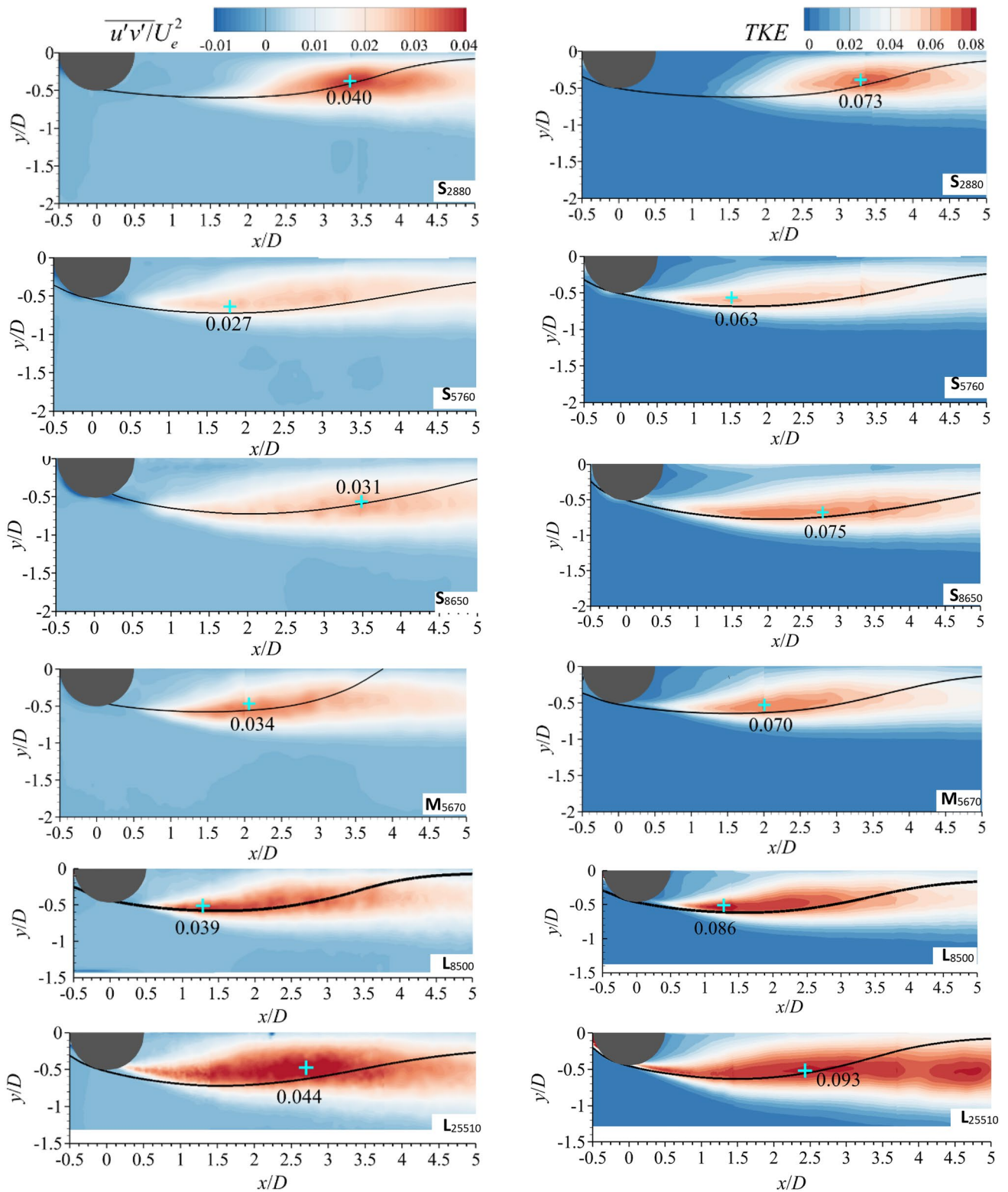


Fig. 7 Contours of Reynolds shear stress (left) and turbulent kinetic energy (right) for selected test cases. The magnitudes of the peak Reynolds shear stress ($\overline{u'v'}/U_e^2$) and turbulent kinetic energy (TKE)

are shown on the contours and their respective locations are marked by the plus “+” symbol. The black solid line is the mean dividing streamline

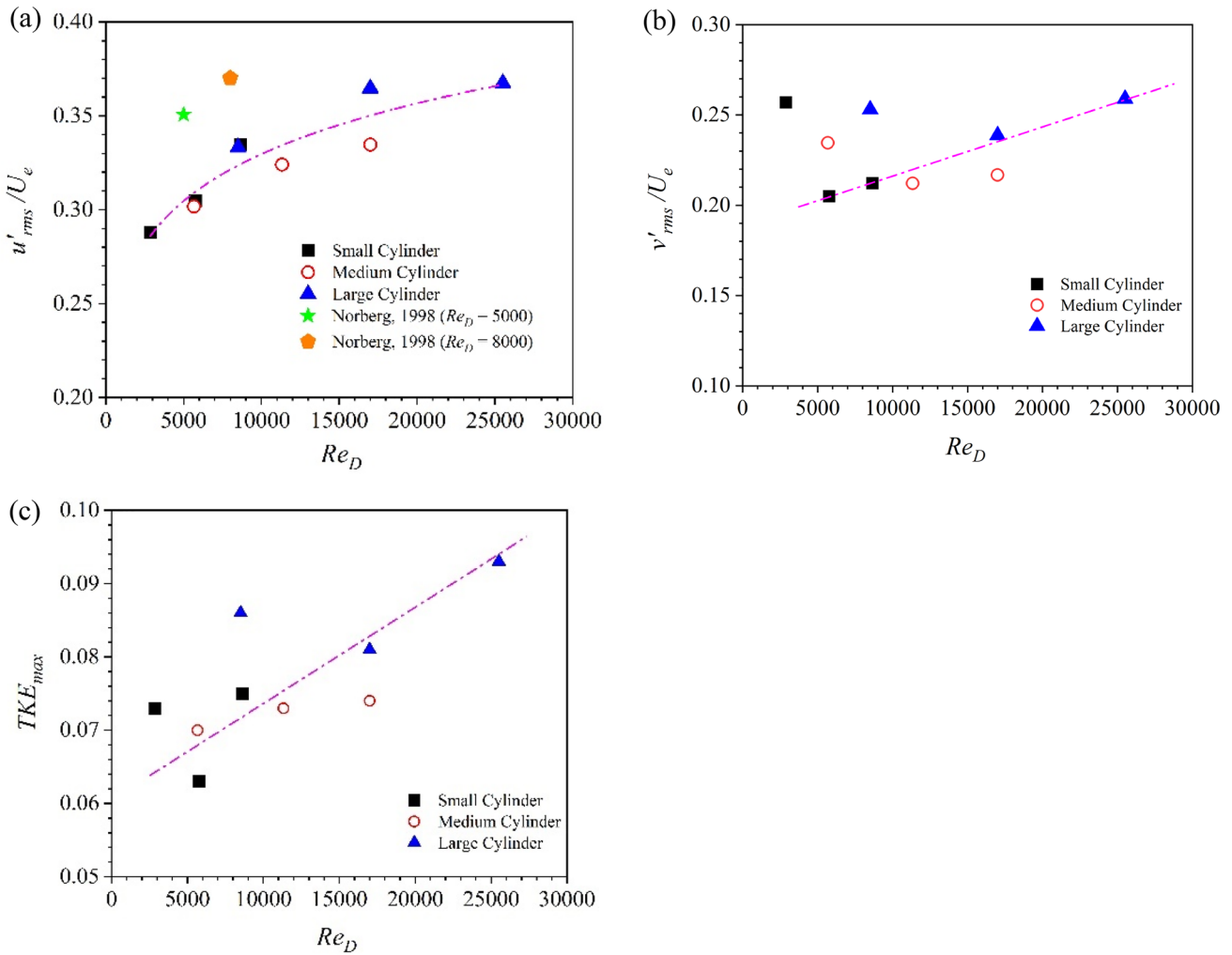


Fig. 8 Plot of root-mean-square values of the **a** streamwise and **b** vertical fluctuating velocities, and **c** TKE versus Reynolds number (Re_D)

where P_k , C_k , D_k and ϵ_k denote the production, convection by the mean flow, diffusion by turbulence, pressure and viscosity, and dissipation of TKE, respectively. In this particular study, only production (P_k), convection (C_k) and diffusion (D_k) are analyzed, while dissipation (ϵ_k) is excluded due to insufficient spatial resolution to resolve the Kolmogorov scales at which turbulence dissipates. Moreover, the flow is statistically homogeneous in the spanwise direction, and the spanwise mean velocity is zero. Since the fluctuating pressure was not measured, its contribution to the diffusion term is neglected. Based on these assumptions and simplifications, the production, convection and diffusion terms are computed using the following expressions:

$$P_k = -\overline{u'u'} \frac{\partial U}{\partial x} - \overline{v'v'} \frac{\partial V}{\partial y} - \overline{u'v'} \frac{\partial U}{\partial y} - \overline{u'v'} \frac{\partial V}{\partial x} \quad (3)$$

$$C_k = -U \frac{\partial k}{\partial x} - V \frac{\partial k}{\partial y} \quad (4)$$

$$D_k = \frac{\partial}{\partial x} \left(\frac{\partial k}{\partial x} - \overline{u'u'u'} - \overline{u'v'v'} \right) + \frac{\partial}{\partial y} \left(\frac{\partial k}{\partial y} - \overline{u'v'v'} - \overline{v'v'v'} \right) \quad (5)$$

Figure 11 shows contours of the production term (P_k) for selected test cases. As shown in the figure, the production term, which is the source of turbulence energy, is positive along the mean dividing streamline where the Reynolds stresses and TKE are greatly enhanced. This observation is consistent with the findings by Cimarelli et al. (2019) and Kumahor (2021) for square and rectangular cylinders in a uniform flow. Also, the peak magnitudes of production for both small and large cylinders increase as Reynolds number increases due to elevated Reynolds normal stresses and TKE with increasing Reynolds number.

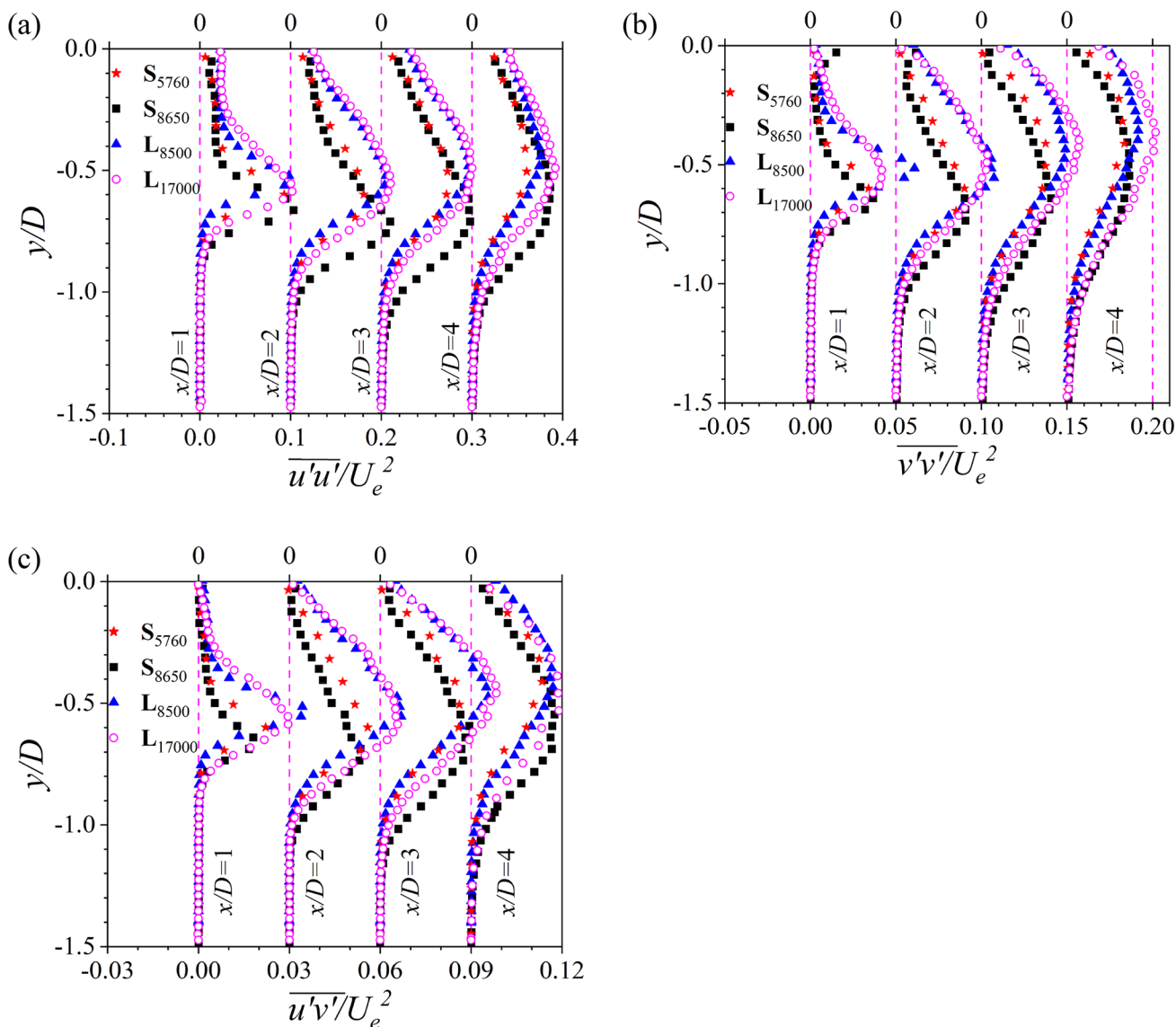


Fig. 9 Vertical profiles of **a** streamwise and **b** vertical Reynolds normal stresses and **c** Reynolds shear stress for some test cases at selected streamwise locations (i.e., $x/D = 1, 2, 3$ and 4). The profiles

at consecutive streamwise locations are shifted to the right of the preceding location for clarity

Unlike the large cylinder, the location where peak production occurs for the small cylinder shifts upstream from $x/D = 3.2$ to $x/D = 1.1$ as Reynolds number increases from $Re_D = 2880$ to 8650 . This observation is consistent with the variation of the Reynolds normal stresses with Reynolds number for the small cylinder and suggests that an increase in Reynolds number promotes early transition to turbulence (Brun et al. 2008; Lander et al. 2018; Moore et al. 2019). The peak magnitude of production decreases with increasing cylinder size at comparable Reynolds number, an indication that blockage affects the turbulence production process. For example, the peak magnitude of S_{5760} is about 106% higher

than that of M_{5670} whereas the peak production of S_{8650} is an order of magnitude higher than that of L_{8500} .

Vertical profiles of the individual production terms and the total production at the peak location of production are presented in Fig. 12a, c, e, g, i to quantitatively examine the relative contributions of the Reynolds normal and shear stresses to the total production. The continuity equation is simplified to $\frac{\partial U}{\partial x} = -\frac{\partial V}{\partial y}$, as the working fluid is not compressible and the mean flow is homogeneous in the spanwise direction. As a consequence, the net contribution from the streamwise Reynolds normal stress ($-u'u' \frac{\partial U}{\partial x}$) and vertical Reynolds normal stress ($-v'v' \frac{\partial V}{\partial y}$) can be combined as $(v'v' - u'u')$

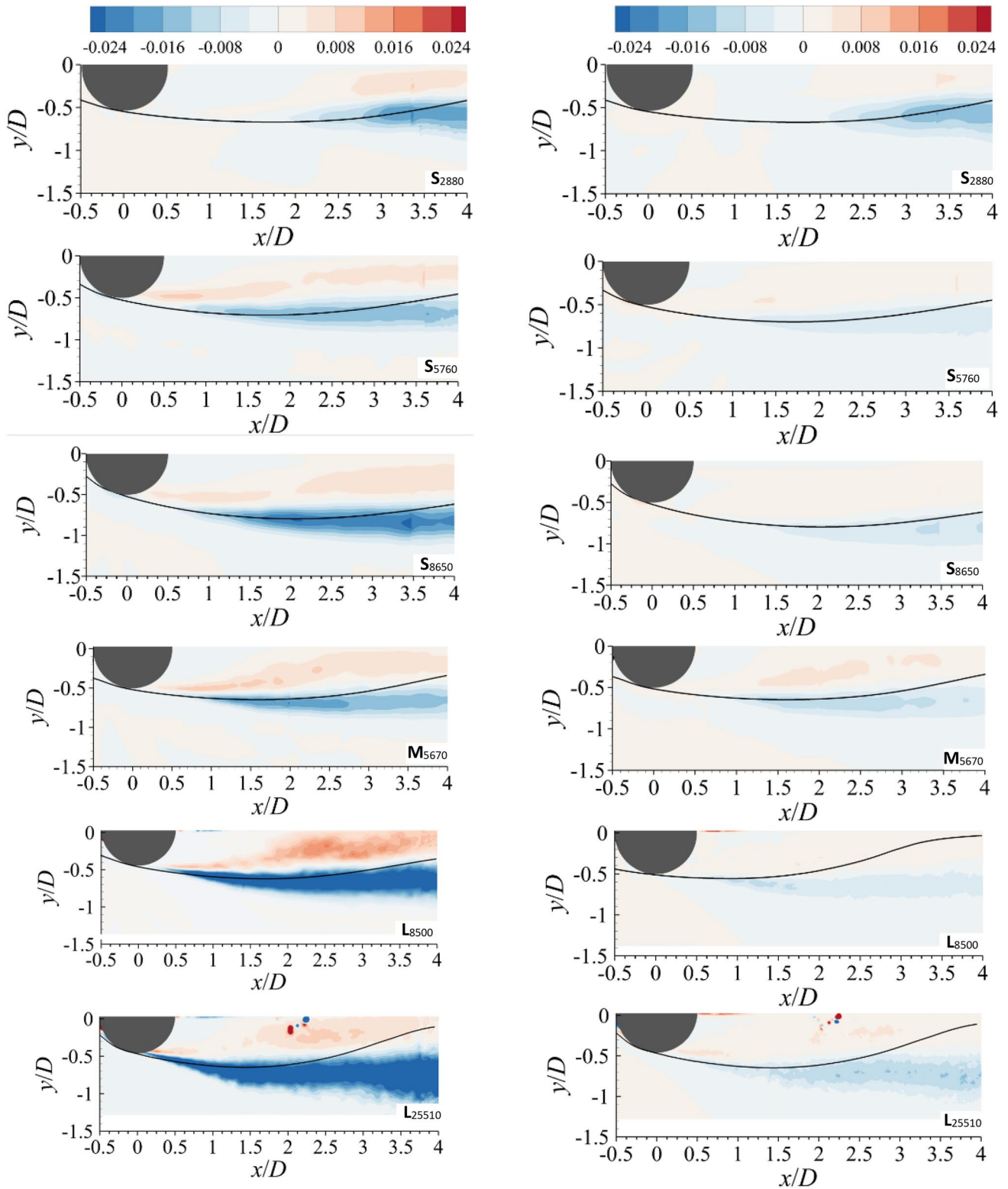


Fig. 10 Contours of triple velocity correlations **a** $\overline{u'u'u'} + \overline{v'v'u'}$ (left) and **b** $\overline{u'u'v'} + \overline{v'v'v'}$ (right) for selected test cases. The black solid line is the mean dividing streamline

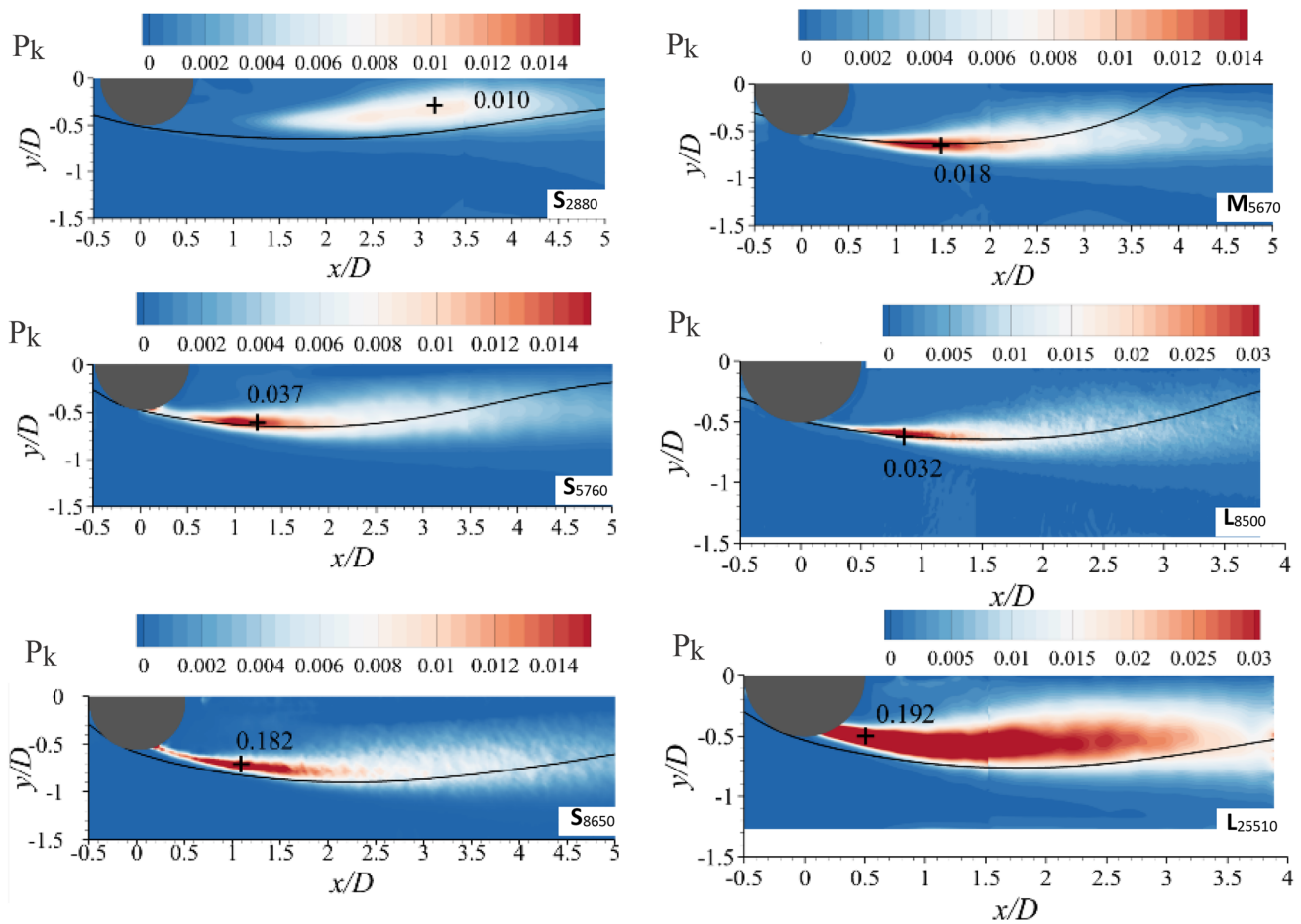


Fig. 11 Contours of the production term for selected test cases at the peak location of the production term which coincides with the peak location of TKE. The black solid line on the contours is the mean dividing streamline

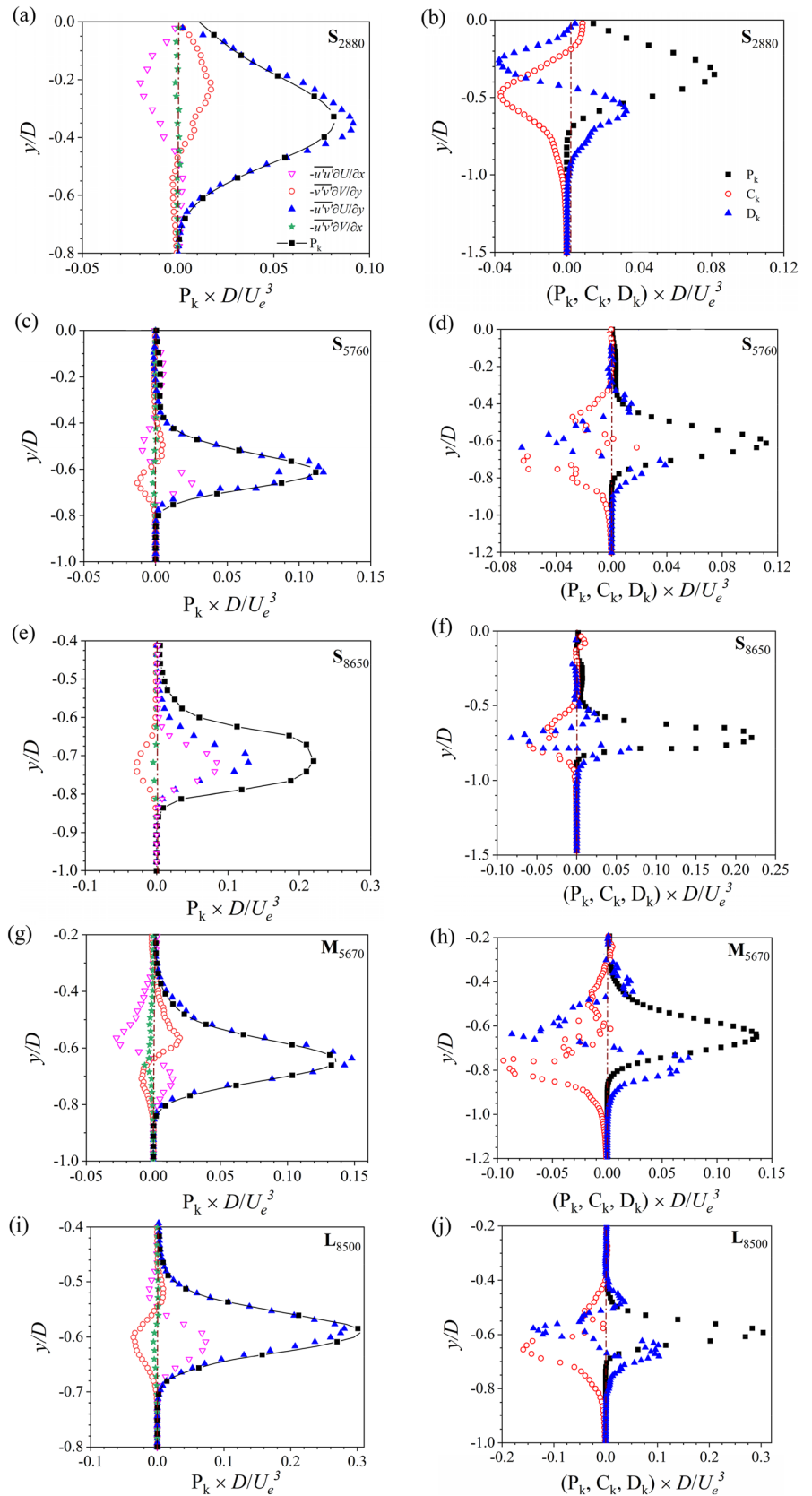
$-\overline{u'u'}$ $\frac{\partial U}{\partial x}$. Since $\overline{u'u'}$ and $\overline{v'v'}$ are always positive, the contribution from the Reynolds normal stresses can act as an energy sink or source depending on their relative magnitude and the sign of $\frac{\partial U}{\partial x}$. For S_{2880} , $\frac{\partial U}{\partial x} > 0$ and since $\overline{v'v'} > \overline{u'u'}$, the net contribution from the Reynolds normal stresses is positive. It is noted that the contribution from $-\overline{u'v'} \frac{\partial V}{\partial x}$ is negligibly small, and $-\overline{u'v'}$ and $\frac{\partial U}{\partial y}$ are both positive, as such $-\overline{u'v'} \frac{\partial U}{\partial y}$ acts as an energy source. Since the contributions from the two Reynolds normal stresses are of opposite signs, and their magnitudes are not significantly different, the total production and $-\overline{u'v'} \frac{\partial U}{\partial y}$ are nearly indistinguishable except in the vicinity of $y/D = -0.4$. For the higher Reynolds number cases as well (Fig. 12c, e, g, i), $-\overline{u'v'} \frac{\partial V}{\partial x}$ is also negligible and $-\overline{u'v'} \frac{\partial U}{\partial y}$ is positive. However, the sign and magnitude of the contributions from the Reynolds normal stresses vary from test case to test case. In the case of S_{5760} , M_{5670} and L_{8500} , for instance, $-\overline{u'u'} \frac{\partial U}{\partial x}$ and $-\overline{v'v'} \frac{\partial V}{\partial y}$ change sign across

the shear layer but because they are of opposite sign and comparable magnitude, their net contribution is sufficiently small that $-\overline{u'v'} \frac{\partial U}{\partial y}$ is the primary source of production.

Unlike S_{2880} , $-\overline{u'u'} \frac{\partial U}{\partial x}$ is positive and $-\overline{v'v'} \frac{\partial V}{\partial y}$ is negative in the case of S_{8650} . Also, $-\overline{u'u'} \frac{\partial U}{\partial x}$ is of larger magnitude than $-\overline{v'v'} \frac{\partial V}{\partial y}$, and comparable to $-\overline{u'v'} \frac{\partial U}{\partial y}$, and as a consequence, the net contribution from the Reynolds stresses to total production is not trivial in this case.

In Fig. 12b, d, f, h, j, vertical profiles of the production, convection, and diffusion terms, as expressed in Eqs. 3–5 are shown to quantitatively assess their relative contributions to the balance of TKE across the separated shear layer. For all test cases, the production term is positive and acts as an energy source whereas the convection term is predominantly negative, acting as a sink. Above $y/D = -0.5$ for S_{2880} , the negative diffusion term together with the convection term acts as a sink to partly balance the positive production. The convection term peaks at $y/D = -0.5$ which coincides with

Fig. 12 Vertical profiles of the **a, c, e, g, i** (left) individual production terms and **b, d, f, h, j** (right) energy budget terms for selected test cases at the peak location of production term which coincides with the peak location of TKE



the upward deflection of the reverse flow. At this vertical location, the diffusion term switches sign to positive and combines with production to balance the negative convection. The switch in sign of the diffusion term as well as its role in the balance of energy for S_{2880} is similar for all other test cases. Also, at comparable Reynolds numbers, the magnitudes of the production, convection and diffusion terms are observed to increase with increasing cylinder size.

3.5 Two-point autocorrelation

To examine the effects of Reynolds number on the large-scale structures, two-point correlation functions are utilized, which are defined as follows:

$$R_{u_i u_j}(x_{ref} + \Delta x, y_{ref} + \Delta y) = \frac{\overline{u'_i(x_{ref}, y_{ref}) u'_j(x_{ref} + \Delta x, y_{ref} + \Delta y)}}{\overline{u'^2_{i,rms}(x_{ref}, y_{ref})} \overline{u'^2_{j,rms}(x_{ref} + \Delta x, y_{ref} + \Delta y)}}, \quad (6)$$

where (x_{ref}, y_{ref}) correspond to the reference point, u_i and u_j are two fluctuating velocities (such as u' and v'), Δx and Δy are the spatial separations between u_i and u_j in the streamwise and wall-normal directions, respectively, and $u'_{i,rms}$ and $u'_{j,rms}$ are, respectively, the root-mean-square values of u_i and u_j at (x_{ref}, y_{ref}) and $(x_{ref} + \Delta x, y_{ref} + \Delta y)$.

Contours of the autocorrelation of streamwise (R_{uu}) and vertical (R_{vv}) velocity fluctuations at selected streamwise locations along the lower separated shear layer are presented in Figs. 13 and 14, respectively. The shapes of R_{uu} and R_{vv} , which are stretched in the longitudinal and transverse directions, are imprints of the large-scale coherent structures (Christensen and Adrian 2001; Christensen and Wu 2005). The asymmetric nature of the R_{uu} and R_{vv} shapes is consistent with previous results for circular, square, and rectangular cylinders as well as forward-facing steps (Perret 2009; Essel and Tachie 2017; Addai et al. 2022; Chalmers et al. 2021). For each test case, the spatial extents of R_{uu} and R_{vv} increase with increasing streamwise distance. The topology of the R_{vv} contours (Fig. 14) show a pattern of alternate regions of positive and negative values centered along the shear layer. Similar results have been reported along the centerline of wake flow generated by a circular cylinder in uniform flow and were attributed to the strong organization of von Kármán vortex street (Tang et al. 2015).

Vertical profiles, extracted in the streamwise and vertical directions through the respective locations or reference points on the R_{uu} and R_{vv} contours for the selected test cases are shown in Fig. 15. The analysis was performed along the shear layer at the following three streamwise locations: $x/D = 1, 2$ and 3 . Except for the large cylinder, the profiles tend to decay faster with increasing downstream distance. Unlike homogeneous turbulent shear flows where such profiles are symmetric with respect to the self-correlation point,

significant differences are observed between the two halves in many cases (see R_{vv} for S_{2880} and M_{5670} , for instance). The integral length scales are typically evaluated by integrating R_{uu} and R_{vv} from the self-correlation point to the point where the profiles go to zero (Ruderich and Fernholz 1986; Addai 2022). Since most of the correlation functions shown in Fig. 15 do not decay to zero, following Volino et al. (2009) and Tay et al. (2013), the length scale of the eddies in the near wake is estimated from these profiles by measuring the longitudinal and transverse distances between the points where the respective correlation coefficients decay to 0.5, as indicated by the arrows on Fig. 15a and d. The longitudinal length scales of the large-scale eddies estimated using this approach at $x/D = 1$ are $L_{-u^x} = 1.0 D, 0.97 D, 0.55 D$ and $0.84 D$ for test cases $S_{2880}, S_{5760}, M_{5670}$ and L_{8500} , respectively. Thus, with increasing Reynolds number, the longitudinal extent of the large-scale eddies increases for the small cylinder but decreases for the large cylinder. In the vertical direction, however, the transverse length scale of the eddies for $S_{2880}, S_{5760}, M_{5670}$ and L_{8500} are, respectively, $L_{-v^y} = 0.72 D, 0.26 D, 0.39 D$ and $0.26 D$. Thus, as Reynolds number increases, the transverse integral length scales in the near-wake region of the small cylinder decrease whereas those for the large cylinder increase.

4 Summary and conclusions

Separated flow around half-submerged horizontal circular cylinders was investigated using particle image velocimetry. Three (3) cylinder geometries with varying sizes were tested at different Reynolds numbers. The results were analyzed in terms of the mean flow, Reynolds stresses, turbulent transport of TKE, energy budget and two-point autocorrelation functions.

The local maximum streamwise mean velocity was observed to increase with increasing Reynolds number. As Reynolds number increased, the maximum back flow and the size of the recirculation bubble behind the small cylinder increased whereas those for the medium and large circular cylinders were nearly independent of Re_D . Also, the maximum back flow was found to increase as cylinder size increased and the vortex core shifted upstream with increasing Reynolds number.

The Reynolds stresses and TKE were concentrated along the mean dividing streamline with single peaks, and the peak locations for the small cylinder moved upstream whereas those of the large cylinder shifted downstream as Reynolds number increased. The topology of the triple velocity correlations also showed concentrations along the mean dividing streamline. Sweep events are the main mechanism by which the fluctuating velocities transport TKE from the mean dividing streamline and towards the free surface

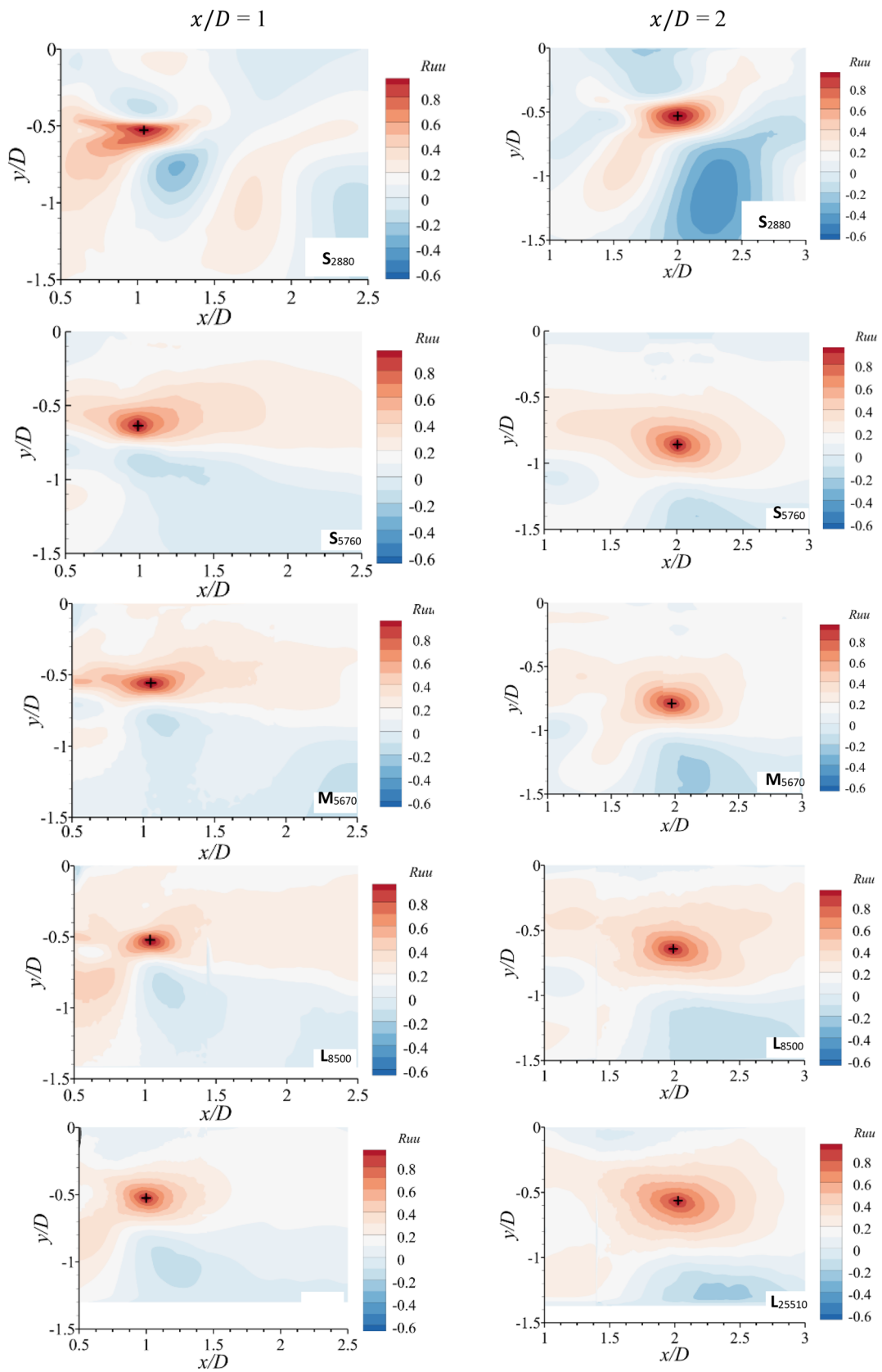


Fig. 13 Contours of R_{uu} for selected test cases along the lower separated shear layer at selected streamwise locations of $x/D = 1$ and 2

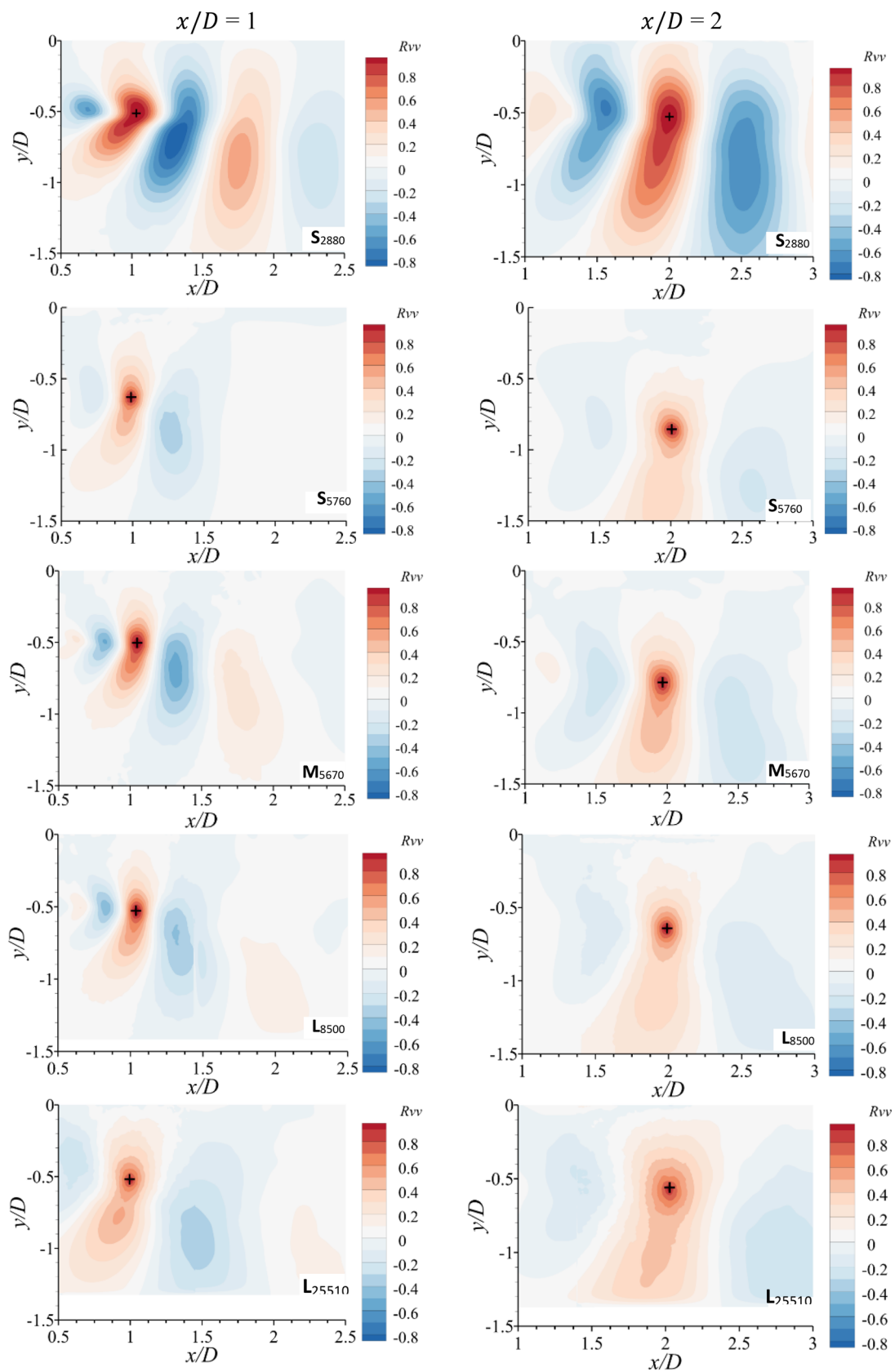


Fig. 14 Contours of R_{vv} for selected test cases along the lower separated shear layer at selected streamwise locations of $x/D = 1$ and 2

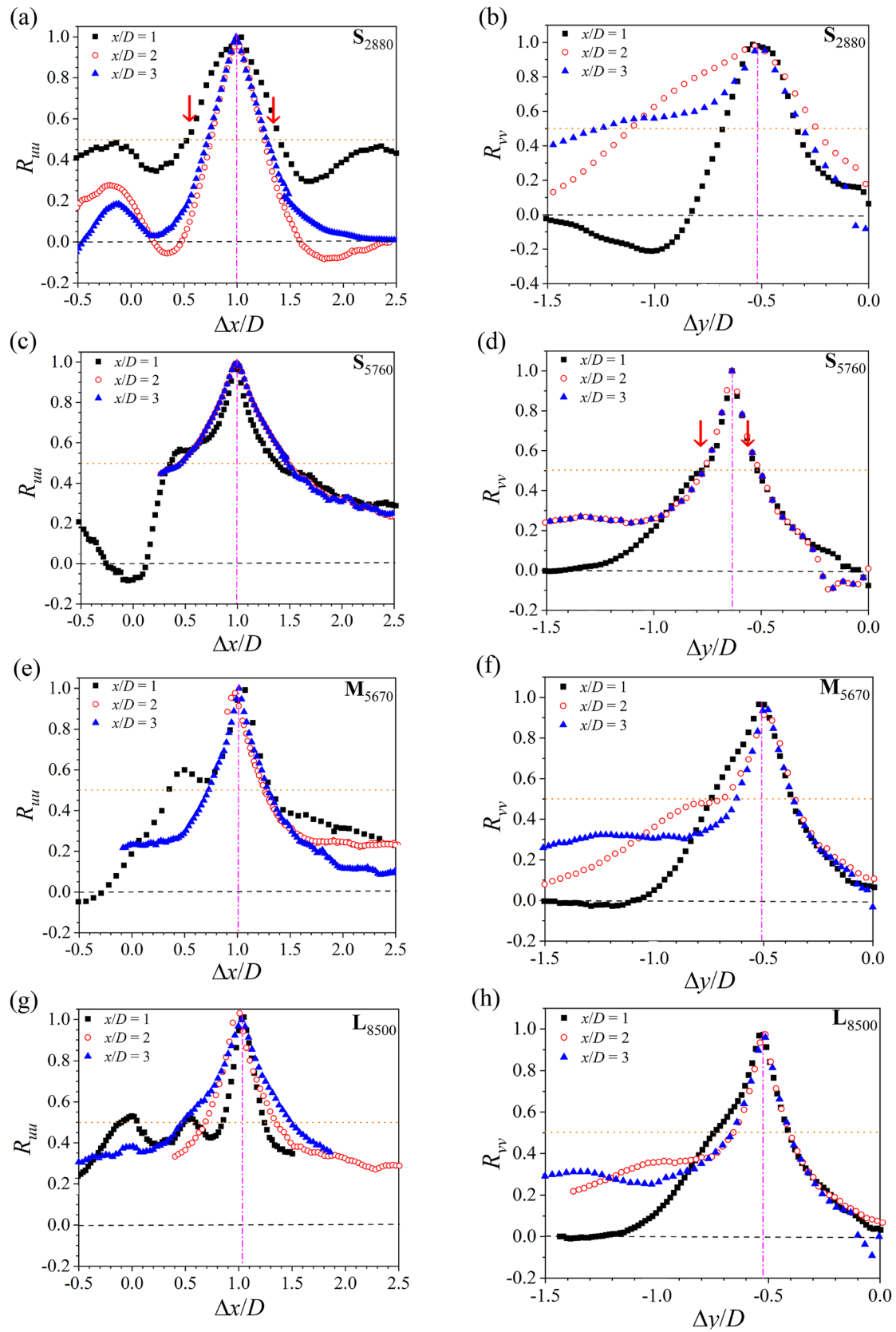


Fig. 15 Vertical profiles of (left) R_{uu} and right (R_{vv}) at selected streamwise locations of $x/D = 1, 2$ and 3 . The x -coordinates of the profiles at $x/D = 2$ and 3 have been shifted to facilitate comparison

whereas turbulent transport from the mean dividing streamline into the outer shear layer is accomplished through ejection events. The transport of TKE by fluctuating streamwise velocity was comparatively more intense than that by the fluctuating vertical velocity for each test case.

The level of turbulence production was found to increase with increasing Reynolds number. Analysis of the individual production terms showed that the dominant contributor to the net production is the shear stress, $-\overline{u'v'} \frac{\partial U}{\partial y}$. The total production and convection terms consistently act as an energy source and sink, respectively, for each test case. As a result, the balance of TKE budget was primarily determined by the diffusion term.

From the two-point autocorrelation analysis, the spatial coherence of the structures was observed to decrease with increase in Reynolds number, for each cylinder geometry. In addition, the longitudinal length of the large-scale eddies for the cylinders were observed to decrease as Reynolds number increased. While it was expected that the wake of a partially submerged circular cylinder would substantially differ from that of the fully immersed cylinder, this study has provided some additional insights into the turbulence characteristics, turbulence transport and spatial characteristics of the distinct vortical structures. Indeed, the findings from this study show that, the variety of turbulent activities in the wake flow of booms ultimately contribute to the unsteady forces imposed on booms and their failure.

Author contributions Conceptualization: KD, SPC, MFT; methodology: SA, MKI, KD, SPC, MFT; formal analysis and investigation: SA, MKI, KD, SPC, MFT; writing and draft preparation: SA, MKI; review: KD, SPC, MFT; funding acquisition: SPC; KD; resources: KD, SPC, MFT; supervision: KD, SPC, MFT.

Funding The funding supports from Manitoba Hydro, the Natural Sciences and Engineering Research Council of Canada (NSERC), and the University of Manitoba are gratefully acknowledged.

Availability of data and materials The datasets are stored on hard drives on the University of Manitoba campus and are readily accessible to the authors.

Declarations

Conflict of interest There are no competing interests.

Ethical approval Not applicable.

References

- Addai S (2022) Experimental study of wall proximity effects on turbulent flow around a square cylinder. M.Sc. thesis, University of Manitoba, Canada
- Addai S, Fang X, Mante AA, Tachie MF (2022) The wake dynamics behind a near-wall square cylinder. *J Fluids Eng* 144:051305–1. <https://doi.org/10.1115/1.4052675>
- Aljure DE, Lehmkhul O, Rodriguez I, Oliva A (2017) Three dimensionality in the wake of the flow around a circular cylinder at Reynolds number 5000. *Comput Fluids* 147:102–118. <https://doi.org/10.1016/j.compfluid.2017.02.004>
- Arie M, Kiya M, Suzuki Y, Hagino M, Takahashi K (1981) Characteristics of circular cylinders in turbulent flows. *Bull JSME* 24:640–647. <https://doi.org/10.1299/jsme1958.24.640>
- Bearman PW, Morel T (1983) Effect of free stream turbulence on the flow around bluff bodies. *Prog Aerosp Sci* 20:97–123. [https://doi.org/10.1016/0376-0421\(83\)90002-7](https://doi.org/10.1016/0376-0421(83)90002-7)
- Bendat JS, Piersol AG (2010) Random data: analysis and measurement procedures, 4th edn. Wiley, Hoboken. <https://doi.org/10.2307/2289430>
- Bhattacharyya S, Maiti DK (2004) Shear flow past a square cylinder near a wall. *Int J Eng Sci* 42:2119–2134. <https://doi.org/10.1016/j.ijengsci.2004.04.007>
- Bouscasse B, Marronen S, Colagrossi A, Souto-Iglesias A (2015) High Froude number viscous flow past a circular cylinder. In: Proceedings of the ASME 34th international conference on ocean, offshore and Arctic Engineering, Newfoundland, Canada. <https://doi.org/10.1115/OMAE2015-41857>
- Brun C, Aubrun S, Goossens T, Ravier Ph (2008) Coherent structures and their frequency signature in the separated shear layer on the sides of a square cylinder. *Flow Turbul Combust* 81:97–114. <https://doi.org/10.1007/s10494-008-9152-4>
- Chalmers H, Fang X, Tachie MF (2021) Streamwise aspect ratio effects on turbulent flow separations induced by forward–backward-facing steps. *J Fluids Eng* 143:021305–021311. <https://doi.org/10.1115/1.4048686>
- Christensen KT, Adrian RJ (2001) Statistical evidence of hairpin vortex packets in wall turbulence. *J Fluid Mech* 431:433–443. <https://doi.org/10.1017/S0022112001003512>
- Christensen KT, Wu Y (2005) Characteristics of vortex organization in the outer layer of wall turbulence. In: Proceedings of fourth international symposium on turbulence and shear flow phenomena, vol 3, Williamsburg, Virginia, pp 1025–1030
- Cimarelli A, Leonforte A, De Angelis E, Crivellini A, Angeli D (2019) On negative turbulence production phenomena in the shear layer of separating and reattaching flows. *Phys Lett A* 383:1019–1026. <https://doi.org/10.1016/j.physleta.2018.12.026>
- Durao DFG, Gouveia PST, Pereira JCF (1991) Velocity characteristics of the flow around a square cross section cylinder placed near a channel wall. *Exp Fluids* 11:341–350. <https://doi.org/10.1007/BF00211788>
- Edie ED (2022) Investigation of the hydraulic effects of ice booms. M.Sc. thesis, University of Manitoba, Canada
- Edie E, Clark S, Dow K (2021) Hydraulic effects of an ice boom in ice-free conditions. CGU HS Committee on river ice processes and the environment, Saskatoon, Saskatchewan, Canada
- Essel EE, Tachie MF (2015) Roughness effects on turbulent flow downstream of a backward facing step. *Flow Turbul Combust* 94:125–153. <https://doi.org/10.1007/s10494-014-9549-1>
- Essel EE, Tachie MF (2017) Upstream roughness and Reynolds number effects on turbulent flow structure over forward-facing step. *Int J Heat Fluid Flow* 66:226–242. <https://doi.org/10.1016/j.ijheatfluidflow.2015.11.004>
- Hammache M, Gharib M (1989) A novel method to promote parallel vortex shedding in the wake of circular cylinders. *Phys Fluids* 1:1611–1614. <https://doi.org/10.1063/1.857306>
- Khabbouchi I, Fellouah H, Ferchichi M, Guellouz MS (2014) Effects of free-stream turbulence and Reynolds number on the separated shear layer from a circular cylinder. *J Wind Eng Ind Aerodyn* 135:46–56. <https://doi.org/10.1016/j.jweia.2014.10.005>

- Kim N, Kim H, Park H (2015) An experimental study on the effects of rough hydrophobic surfaces on the flow around a circular cylinder. *Phys Fluids* 27:085113. <https://doi.org/10.1063/1.4929545>
- Kumahor S (2021) Spatio-temporal characteristics of turbulent flow around rectangular cylinders subject to varying oncoming flow conditions. M.Sc. thesis, University of Manitoba, Canada
- Lander DC, Moore DM, Letchford CW, Amitay M (2018) Scaling of square-prism shear layers. *J Fluid Mech* 849:1096–1119. <https://doi.org/10.1017/jfm.2018.443>
- Lei C, Cheng L, Kavanagh K (1999) Re-examination of the effect of a plane boundary on force and vortex shedding of a circular cylinder. *J Wind Eng Ind Aerodyn* 80:263–286. [https://doi.org/10.1016/S0167-6105\(98\)00204-9](https://doi.org/10.1016/S0167-6105(98)00204-9)
- Lin J-C, Towfighi J, Rockwell D (1995) Instantaneous structure of the near-wake of a circular cylinder: on the effect of Reynolds number. *J Fluids Struct* 9:409–418. <https://doi.org/10.1006/jfls.1995.1023>
- Lin J-C, Sheridan J, Rockwell D (1996) Near-wake of a perturbed, horizontal cylinder at a free-surface. *Phys Fluids* 8:2107. <https://doi.org/10.1063/1.868985>
- Maekawa T, Mizuno S (1967) Flow around the separation point and in the near-wake of a circular cylinder. *Phys Fluids* 10:S184. <https://doi.org/10.1063/1.1762442>
- Martinuzzi RJ, Bailey SCC, Kopp GA (2003) Influence of wall proximity on vortex shedding from a square cylinder. *Exp Fluids* 34:585–596. <https://doi.org/10.1007/s00348-003-0594-0>
- Moore DM, Letchford CW, Amitay M (2019) Energetic scales in a bluff body shear layer. *J Fluid Mech* 875:543–575. <https://doi.org/10.1017/jfm.2019.480>
- Norberg C (1986) Interaction between freestream turbulence and vortex shedding for a single tube in cross-flow. *J Wind Eng Ind Aerodyn* 23:501–514. [https://doi.org/10.1016/0167-6105\(86\)90066-8](https://doi.org/10.1016/0167-6105(86)90066-8)
- Norberg C (1998) LDV-measurements in the near wake of a circular cylinder. In: *Advances in understanding of bluff body wakes and vortex-induced vibration*
- Perret L (2009) PIV investigation of the shear layer vortices in the near wake of a circular cylinder. *Exp Fluids* 47:789–800. <https://doi.org/10.1007/s00348-009-0665-y>
- Price SJ, Sumner D, Smith JG, Leong K, Paidoussis MP (2002) Flow visualization around a circular cylinder near to a plane wall. *J Fluids Struct* 16(2):175–191. <https://doi.org/10.1006/jfls.2001.0413>
- Qiu X, Sun W, Tao Y, Li J, Li J, Liu Y (2022) Large eddy simulation of structural characteristics in turbulent flow around a circular cylinder close to a wavy wall. *AIP Adv* 12:065204
- Reichl P, Hourigan K, Thompson M (2003) The unsteady wake of a circular cylinder near a free surface. *Flow Turbul Combust* 71:347–359. <https://doi.org/10.1023/B:APPL.0000014926.99751.b1>
- Ruderich R, Fernholz HH (1986) An experimental investigation of a turbulent shear flow with separation, reverse flow, and reattachment. *J Fluid Mech* 163:283–322. <https://doi.org/10.1017/S0022112086002306>
- Samimy M, Lele SK (1991) Motion of particles with inertia in a compressible free shear layer. *Phys Fluids A* 3(8):1915–1923. <https://doi.org/10.1063/1.857921>
- Sciacchitano A, Wieneke B (2016) PIV uncertainty propagation. *Meas Sci Technol* 27:084006
- Sheridan J, Lin J-C, Rockwell D (1997) Flow past a cylinder close to a free surface. *J Fluid Mech* 330:1–30
- Sherry M, Lo Jacono D, Sheridan J (2009) Flow separation characterisation of a forward-facing step immersed in a turbulent boundary layer. In: *Sixth international symposium on turbulence and shear flow phenomena*, Seoul, Korea
- Tang SL, Djenidi L, Antonia RA, Zhou Y (2015) Comparison between velocity-and vorticity-based POD methods in a turbulent wake. *Exp Fluids* 56:169. <https://doi.org/10.1007/s00348-015-2038-z>
- Taniguchi S, Miyakoshi K (1990) Fluctuating fluid forces acting on a circular cylinder and interference with a plane wall: effects of boundary layer thickness. *Exp Fluids* 9:197–204. <https://doi.org/10.1007/BF00190418>
- Tay GFK, Kuhn DCS, Tachie MF (2013) Surface roughness effects on the turbulence statistics in a low Reynolds number channel flow. *J Turbul* 14:121–146. <https://doi.org/10.1080/14685248.2012.737468>
- Thompson MC, Leweke T, Hourigan K (2020) Bluff bodies and wake-wall interactions. *Annu Rev Fluid Mech* 53:347–376. <https://doi.org/10.1146/annurev-fluid-072220-123637>
- Triantafyllou GS, Dimas AA (1989) Interaction of two-dimensional separated flows with a free surface at low Froude numbers. *Comput Fluids* 1(11):1813–1821. <https://doi.org/10.1063/1.857507>
- Uruba V (2022) Wake behind a cylinder: an overview of the spatio-temporal aspects. In: *27/28th international conference engineering mechanics*, vol 112, pp 7–14. <https://doi.org/10.21495/5127>
- Volino RJ, Schultz MP, Flack KA (2009) Turbulence structure in a boundary layer with two-dimensional roughness. *J Fluid Mech* 635:75–101. <https://doi.org/10.1017/S0022112009007617>
- Wang XK, Tan SK (2008) Comparison of flow patterns in the near wake of a circular cylinder and a square cylinder placed near a plane wall. *Ocean Eng* 35:458–472. <https://doi.org/10.1016/j.oceaneng.2008.01.005>
- Zdravkovich MM (1985) Forces on a circular cylinder near a plane wall. *Appl Ocean Res* 7:197–201. [https://doi.org/10.1016/0141-1187\(85\)90026-4](https://doi.org/10.1016/0141-1187(85)90026-4)
- Zdravkovich MM (1997) Flow around circular cylinders. In: *Fundamentals*, vol 1. Oxford University Press, Oxford, Chapter 6
- Zovatto L, Pedrizzetti G (2001) Flow about a circular cylinder between parallel walls. *J Fluid Mech* 440:1–25. <https://doi.org/10.1017/S0022112001004608>

Publisher's Note Springer Nature remains neutral with regard to jurisdictional claims in published maps and institutional affiliations.

Springer Nature or its licensor (e.g. a society or other partner) holds exclusive rights to this article under a publishing agreement with the author(s) or other rightsholder(s); author self-archiving of the accepted manuscript version of this article is solely governed by the terms of such publishing agreement and applicable law.